

# Systematic Study of Acceleration Efficiency in Young Supernova Remnants with Nonthermal X-ray Observations

NAOMI TSUJI,<sup>1,2</sup> YASUNOBU UCHIYAMA,<sup>2,3</sup> DMITRY KHANGULYAN,<sup>2</sup> AND FELIX AHARONIAN<sup>4,5</sup>

<sup>1</sup>*Interdisciplinary Theoretical & Mathematical Science Program (iTHEMS), RIKEN, 2-1 Hirosawa, Saitama 351-0198, Japan*

<sup>2</sup>*Department of Physics, Rikkyo University, 3-34-1 Nishi Ikebukuro, Toshima-ku, Tokyo 171-8501, Japan*

<sup>3</sup>*Department of Artificial Intelligence and Science, Rikkyo University, 3-34-1 Nishi Ikebukuro, Toshima-ku, Tokyo 171-8501, Japan*

<sup>4</sup>*Dublin Institute for Advanced Studies, 31 Fitzwilliam Place, Dublin 2, Ireland*

<sup>5</sup>*Max-Planck-Institut für Kernphysik, P.O. Box 103980, D 69029 Heidelberg, Germany*

## ABSTRACT

Cutoff energy in a synchrotron radiation spectrum of an supernova remnant (SNR) contains a key parameter of ongoing particle acceleration. We systematically analyze 11 young SNRs, including all historical SNRs, to measure the cutoff energy, thus shedding light on the nature of particle acceleration at the early stage of SNR evolution. The nonthermal (synchrotron) dominated spectra in filament-like outer rims are selectively extracted and used for spectral fitting because our model assumes that accelerated electrons are concentrated in the vicinity of the shock front due to synchrotron cooling. The cutoff energy parameter ( $\varepsilon_0$ ) and shock speed ( $v_{\text{sh}}$ ) are related as  $\varepsilon_0 \propto v_{\text{sh}}^2 \eta^{-1}$  with a Bohm factor of  $\eta$ . Five SNRs provide us with spatially resolved  $\varepsilon_0$ - $v_{\text{sh}}$  plots across the remnants, indicating a variety of particle acceleration. With all SNRs considered together, the systematic tendency of  $\eta$  clarifies a correlation between  $\eta$  and an age of  $t$  (or an expansion parameter of  $m$ ) as  $\eta \propto t^{-0.4}$  ( $\eta \propto m^4$ ). This might be interpreted as the magnetic field becomes more turbulent and self-generated, as particles are accelerated at a greater rate with time. The maximum energy achieved in SNRs can be higher if we consider the newly observed time dependence on  $\eta$ .

**Keywords:** acceleration of particles — ISM: supernova remnants — radiation mechanisms: non-thermal — X-rays: ISM

## 1. INTRODUCTION

are believed to be prominent accelerators of the galactic with energies up to a few PeV. Under the conditions typical for shocks in SNRs, should be capable of boosting protons to the PeV energies. The rate of in the Galaxy and their typical energy output are high enough to explain the entire flux of PeV CR particles at the Earth. It favors the scenario where the dominant fraction of CRs below the knee is produced in Galactic SNRs. However, this scenario contains some problems, among which the absence of any empirical evidence for existence of PeV particles in SNRs is the most critical. Nearly all SNRs detected in gamma-ray show power-law energy spectra with cutoffs at energies of at most tens of TeV. Thus, it is questionable whether SNRs are indeed capable of producing PeV particles (i.e., whether they are “PeVatron”). From the theoretical point of view, the maximum attainable energy for particles accelerated by DSA in SNRs is not well constrained because of some unknown physical parameters such as a diffusion coefficient of the non-thermal particle and magnetic field turbulence.

In DSA, which is widely accepted as the main acceleration mechanism in SNRs, particles gradually gain energy by crossing the shock wave forward and backward. A particle changes its direction by being scattered by magnetic field. Assuming Bohm diffusion, one can characterize the diffusion coefficient using mean free path that is represented by the product of the particle gyroradius and energy independent factor  $\eta$  (the so-called Bohm factor). In the case of  $\eta = 1$  (also known as the Bohm limit), particle mean free path takes the minimum value, and the particles are accelerated most efficiently. The diffusion coefficient (or the  $\eta$  parameter) is strongly related to the spectrum of

the turbulent magnetic field that scatters particles. Theoretical studies and numerical simulations propose that the turbulence is generated by the instability resulting from the pressure gradient derived from CR streaming (e.g., Bell (1978); Caprioli & Spitkovsky (2014a)). However, many facets of the mechanism of turbulent production are poorly understood.

Synchrotron radiation is a good channel to trace electron acceleration at shocks in SNRs. The synchrotron X-ray, in particular, is emitted by multi-TeV electrons. Therefore, an observation of synchrotron radiation in the X-ray domain is a great means for diagnosing the nature of the acceleration and of the maximum energy attainable in SNRs. In young SNRs where the shock speed is high, the conditions for particle acceleration are especially favorable. Thus, young SNRs, with ages less than a few thousand years, are expected to radiate synchrotron X-rays. The detection of the synchrotron emission has been reported in a few tens of galactic SNRs to date.

One can indirectly estimate  $\eta$  from measuring the shock speed and cutoff energy in the synchrotron X-ray spectrum (e.g., Reynolds (1998); Zirakashvili & Aharonian (2007)). RX J1713.7–3946, an TeV emitting SNR, is recognized as an accelerator operating at the most efficient rate (i.e., the acceleration proceeds in a regime close to the Bohm limit of  $\eta = 1$  (Tanaka et al. 2008; Tsuji et al. 2019)). Since *NuSTAR* was launched in 2012, it has provided us with spatially resolved hard X-ray spectra, thus enabling precise measurements of the cutoff energy. Although young SNRs are believed to be efficient accelerators, some recent observations with *NuSTAR* have in fact revealed that the acceleration efficiency  $\eta$  varies significantly and depends on the acceleration site and/or the object. Based on *NuSTAR* observations, it has been determined that  $\eta$  is  $\sim 1$  in the forward shock and 3–8 in the reverse shock or reflection shock in Cassiopeia A (Sato et al. 2018). In addition,  $\eta$  turned out to be  $\sim 20$  in the youngest galactic SNR, G1.9+0.3 (Aharonian et al. 2017). Toward a unified understanding of the particle acceleration in young SNRs, gaps between G1.9+0.3 ( $\sim 190$  year), Cassiopeia A ( $\sim 330$  year), and RX J1713.7–3946 ( $\sim 1600$  year) must be filled.

In this paper, we present a systematic analysis and measurement of the cutoff energy in the synchrotron radiation spectrum of young 11 SNRs: G1.9+0.3, Cassiopeia A, Kepler’s SNR (hereafter Kepler), Tycho’s SNR (Tycho), G330.2+1.0, SN 1006, RX J1713.7–3946, RCW 86, Vela Jr., HESS J1731–347, and SN 1987A. Most of them are historical, and thus their ages are well constrained. The dataset of observations analyzed here and the data reduction are presented in Section 2. Section 3 presents imaging and spectral analyses. The results are presented in Section 4. Our analysis for the first time reveals a variety of instances of particle acceleration in the remnants and clarifies a systematic tendency of acceleration efficiency. Discussion and interpretation are given in Section 5, and conclusion are provided in Section 6.

## 2. OBSERVATIONS AND DATA REDUCTION

We systematically studied eleven young SNRs using X-ray observations. To reveal a tendency of acceleration efficiency in the young SNRs, they should be strong synchrotron emitters, and their physical parameters, such as age, distance, and shock speed, should be well constrained. The following 11 SNRs were selected based on the aforementioned criteria: G1.9+0.3, Cassiopeia A, Kepler, Tycho, G330.2+1.0, SN 1006, RX J1713.7–3946, RCW 86, Vela Jr., and HESS J1731–347 in our galaxy, and SN 1987A in the . The other candidates that are dominated by synchrotron radiation in the X-ray energy band (e.g., G32.45+0.1 and HESS J1640–465) were not included because there are large uncertainties regarding their ages and distances. The known parameters of the 11 SNRs are listed in Table 1.

We utilized archival X-ray observations using *Chandra* and *NuSTAR*. The dataset used in the analysis is summarized in Table 4 and Table 5 in Section A.

We reduced all the observational data using the following software and calibration. The *Chandra* data were processed using CALDB version 4.8.3 in CIAO version 4.11. The *NuSTAR* data were calibrated and screened using *nupipeline* of *NuSTAR Data Analysis Software* (NuSTARDAS version 1.4.1 with CALDB version 20180814) included in HEASoft version 6.19. To screen the *NuSTAR* data, we used the strictest mode (SAAMODE = STRICT and TENTACLE = YES cut). The effective observational time reduced by these processes is shown in Table 4 and Table 5 (Section A).

## 3. ANALYSIS

### 3.1. Image

Figure 1 illustrates flux images taken with *Chandra*. The energy band is set to be 0.5–7 keV for synchrotron dominated SNRs (i.e., G1.9+0.3, G330.2+1.0, SN 1006, and HESS J1731–347) and RCW 86, while is set to be 4–6 keV for SNRs which contain thermal emissions (i.e., Cassiopeia A, Kepler, and Tycho). All the epochs were combined by using *merge\_obs*, the exposure was corrected, and the background was not subtracted. Note that we show the

**Table 1.** Properties of SNRs analyzed in this paper

Name	Age (yr)	$m^\dagger$	Distance (kpc)	Shock speed (km s $^{-1}$ )	References
G1.9+0.3	190±50	1.1±0.2	~8.5	3600–13000	Borkowski et al. (2010, 2017)
Cassiopeia A (SN 1680)	335±20	0.7±0.1	3.4	4400–5500	Patnaude & Fesen (2009)
Kepler (SN 1604)	415	0.47–0.82	4±1	3400–5700	Cassam-Chenaï et al. (2004); Katsuda et al. (2008b)
Tycho (SN 1572)	440	0.6±0.1	2.3	3200–4000	Williams et al. (2013)
G330.2+1.0	700±300	0.9±0.3	~5	3700–9100	Park et al. (2006); Borkowski et al. (2018)
SN 1006	1010	0.5±0.1	1.9±0.3	3000–7200	Winkler et al. (2014)
RX J1713.7–3946 (SN 393)	1600 ±10	0.7±0.1	1	800–4000	Tsuji & Uchiyama (2016); Acero et al. (2017)
RCW 86 (SN 185)	1835	0.3±0.1	2.8	1800–3000	Rosado et al. (1996); Yamaguchi et al. (2016)
Vela Jr.	3000±1000	0.5±0.2	0.5–0.9	~2000	Allen et al. (2015)
HESS J1731–347	2500–14000	0.5±0.1	3.6±0.4	~2500	H. E. S. S. Collaboration et al. (2011)
SN 1987A	30	0.9±0.1	51.4	~6700	Frank et al. (2016)

NOTE— $^\dagger$  Expansion parameter (i.e.,  $R \propto t^m$  where  $R$  and  $t$  are the radius of the SNR and time from the explosion, respectively).

images of the entire remnants taken with *XMM-Newton* and *Suzaku* for RX J1713.7–3946 and Vela Jr., respectively. We omitted the image of SN 1987A since it is treated as a point-like source in this paper, although it shows spatial extent (e.g., McCray & Fransson (2016)).

Some SNRs have strong thermal line emissions in addition to the synchrotron component, making it difficult to extract the pure synchrotron spectrum. For SNRs that have thermal components, the 4–6 keV channel can be dominated by nonthermal radiation, while the other X-ray band can be contaminated by thermal line emissions. The rims or the filament-like structures, which are likely located in the outermost regions, appear bright in the 4–6 keV energy range (Figure 1). These regions are expected to contain the synchrotron emission from electrons accelerated at the forward shock, and are thus the best targets for our analysis to study particle acceleration in SNRs. We defined regions to extract the spectra along these outer rims (Figure 1). In order to investigate the relation between the shock velocity and synchrotron radiation, we also defined subregions along the regions where the proper motions were measured in the previous works. Five SNRs were picked up for this purpose: proper motions along the entire rims were already measured in G1.9+0.3 (Borkowski et al. 2017), Cassiopeia A (Patnaude & Fesen 2009), Kepler (Katsuda et al. 2008b), Tycho (Williams et al. 2013), and SN 1006 (Winkler et al. 2014). It should be noted that the superb angular resolution of *Chandra* enabled us to extract spectra from relatively small (a few arcsec scale) subregions.

### 3.2. Spectrum

To extract spectra, we used `specextract` and `nuproducts` for *Chandra* and *NuSTAR* data, respectively. The source regions are shown in Figure 1, while the background spectra are extracted from nearby regions of the source otherwise mentioned. The “extended=yes” set was applied to all the *NuSTAR* spectra except for SN 1987A, which is spatially compatible with a point-like source. The spectra of different epochs and different detector modules were combined using `addascaspec`. Although most of the SNRs examined in this paper showed expanding motions, we could safely combine the spectra of the different epochs because the extracted regions were substantially larger than the shifts due to their proper motions. It also should be noted that summing up the spectra of the different epochs is not affected by time evolution and variations across the of the response files. We checked this by simultaneously fitting the spectra of the different epochs, showing the consistent result with when fitting the combined spectrum. The spectra obtained from the representative regions of each SNR are shown in Figure 2.

In many cases *NuSTAR* spectra contain uncertainties related to stray light. We therefore used *NuSTAR* data only for sources which it can be reliably dealt with: namely, for G1.9+0.3, Cassiopeia A (the SE and NE regions), SN 1006 (the subregions 2–4 in NE and 11–13 in SW), RX J1713.7–3946, Vela Jr., and SN 1987A. The background spectrum with *NuSTAR* here does include uncertainty of non-uniform distribution due to stray light and instrumental components (Wik et al. 2014), except for RX J1713.7–3946 which the background was adequately subtracted as reported in

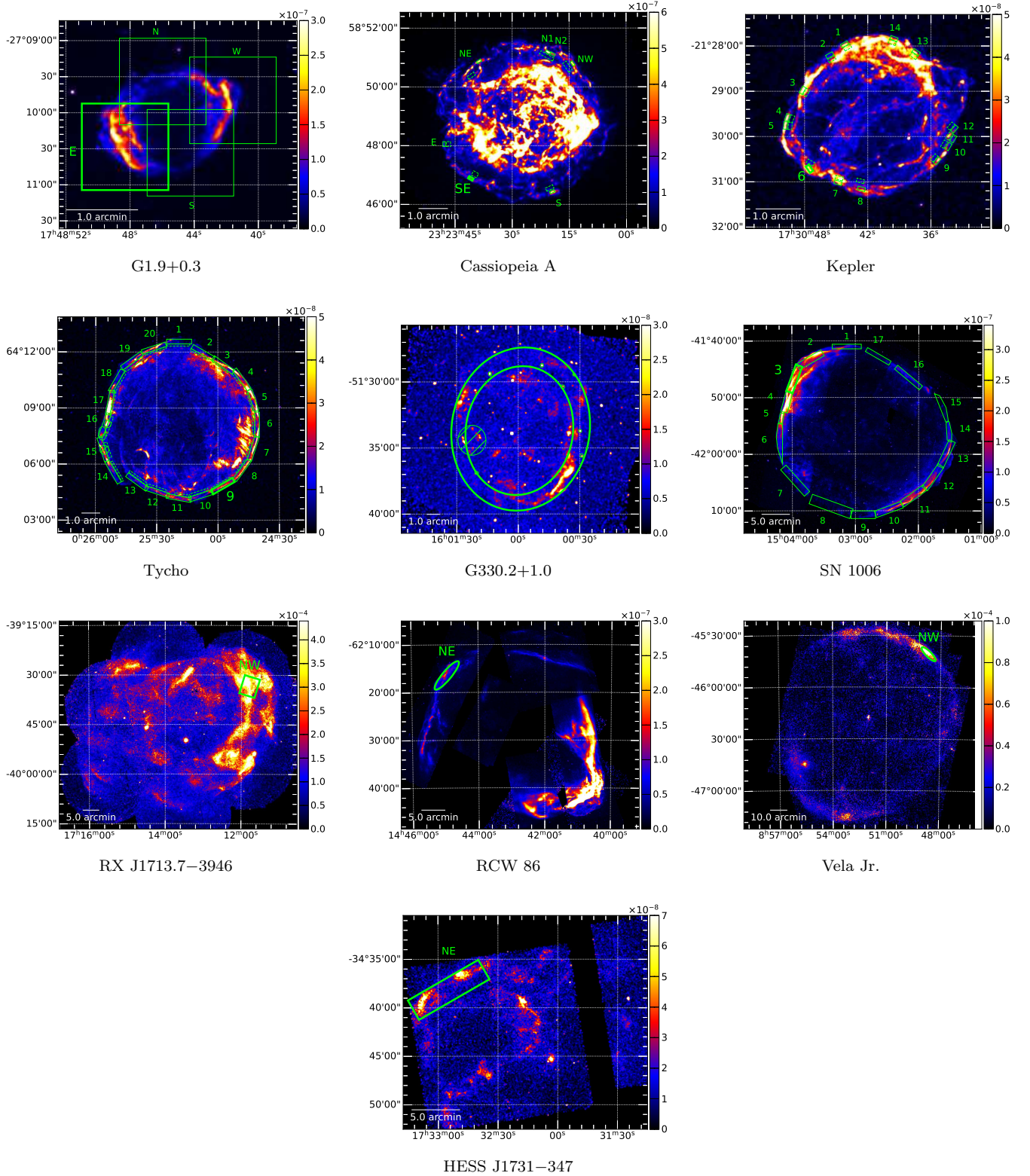


**Figure 1.** Flux images in nonthermal dominated energy bands taken with *Chandra*, except for RX J1713.7–3946 and Vela Jr. taken with *XMM-Newton* and *Suzaku*, respectively. The color map is in units of photons  $\text{cm}^{-2} \text{s}^{-1}$ . 1 pixel corresponds to  $1''$ , except for  $5''$  in RX J1713.7–3946 and  $8''$  in Vela Jr. The region highlighted by the thick line is used in the analysis in Section 4.2. The dashed boxes in Cassiopeia A, Kepler, and Tycho indicate the reference regions used for determination of thermal components (see Section 3.2).



Tsuji et al. (2019). As G1.9+0.3 and SN 1987A have small angular sizes, the background can be extracted from the surrounding region of the source, and the non-uniform distribution of the background should not noticeably affect the results. For largely extended sources, such as SN 1006, RX J1713.7–3946, and Vela Jr., a careful treatment with the non-uniform background is necessary. See Grefenstette et al. (2014), Li et al. (2018) and Tsuji et al. (2019) for the detailed studies of the background spectra in *NuSTAR* observations of Cassiopeia A, SN 1006, and RX J1713.7–3946, respectively. In the case of the *NuSTAR* spectrum of Vela Jr., we simply checked that changing normalization of the present background by  $\pm 10\%$  and  $20\%$  resulted in differences in the spectral parameters within  $7\%$  and  $15\%$ , respectively.

### 3.3. Model

We applied the model of synchrotron radiation from cooling-limited electrons, as proposed in Zirakashvili & Aharonian (2007) (hereafter the ZA07 model), given by

$$\frac{dN_X}{d\varepsilon} \propto \left(\frac{\varepsilon}{\varepsilon_0}\right)^{-2} \left[1 + 0.38 \left(\frac{\varepsilon}{\varepsilon_0}\right)^{1/2}\right]^{11/4} \exp\left[-\left(\frac{\varepsilon}{\varepsilon_0}\right)^{1/2}\right], \quad (1)$$

with  $\varepsilon_0$  being a cutoff energy parameter. In this model, we adopted the  $\kappa = \sqrt{1/11}$  case in which  $\kappa$  is the ratio of the upstream magnetic field to the downstream magnetic field,  $\kappa = B_{\text{up}}/B_{\text{down}}$ . This corresponds to an enhancement of random isotropic magnetic field due to the standard shock compression ratio of  $\sigma = 4$ .

The model is described with an absorbed ZA07, where the interstellar absorption is considered by the TBabs model in XSEPC. The energy band of the *Chandra* spectra is set to be 0.5–7 keV unless otherwise mentioned. For the *NuSTAR* spectra, the energy band is set to be 3–20 keV for SN 1006, RX J1713.7–3946, and Vela Jr.; 3–40 keV for G1.9+0.3 and SN 1987A; and 3–50 keV for Cassiopeia A. We performed spectral fitting of the broadband X-ray observations (i.e., *Chandra* + *NuSTAR* joint fitting) if *NuSTAR* data are available. Although the combination of the *Chandra* and *NuSTAR* spectra gives us the more precise measurement of  $\varepsilon_0$ , the fitting result with solely the *Chandra* data would be less affected by systematic errors. We confirmed this by measuring the  $\varepsilon_0$  parameter separately using only the *Chandra* and *NuSTAR* spectra, showing the consistent results with those obtained by the joint fit. The fitting results are presented in Figure 2 and Table 2. Spectral fitting was performed using XSPEC version 12.9.0.

#### 3.3.1. Synchrotron dominated spectra

X-ray spectra can constrain the process of particle acceleration in SNRs where the synchrotron emission dominates. Such completely featureless and nonthermal spectra were obtained from G1.9+0.3, G330.2+1.0, RX J1713.7–3946, Vela Jr., and HESS J1731–347<sup>1</sup>. They are well reproduced by the absorbed ZA07 model.

On the other hand, some spectra contain non-negligible thermal emission in Cassiopeia A, Kepler, Tycho, SN 1006, RCW 86, and SN 1987A. For these SNRs, we added a thermal model, namely, TBabs  $\times$  (ZA07 + thermal plasma). The thermal model is described by VNEI for Cassiopeia A, Kepler, and Tycho, and by Vpshock in SN 1006 and RCW 86. We added two-component thermal plasma, Vpshock and Vequil, in SN 1987A (see, e.g., Frank et al. 2016). In the former three remnants, a plasma temperature ( $kT$ ) and an ionization parameter ( $nt$ ) are fixed to the values which are derived from the reference regions in Figure 1. Thermal parameters are fixed to the values in the literature for SN 1006 (Miceli et al. 2009), RCW 86 (Tsubone et al. 2017), and SN 1987A (Frank et al. 2016). Additional line emissions described by Gaussian are added when necessary. The parameters of the thermal component are summarized in Table 6 (Section B). Although the spectra are well fitted with this model, X-rays in the higher energy range might originate from thermal Bremsstrahlung and/or a hot plasma instead of synchrotron radiation. Therefore, we defined *synchrotron dominated* spectra as those which 1.) were featureless (i.e., line emissions are weak), and 2.) the normalization ratio of the synchrotron model to the thermal model was relatively large. The threshold normalization ratio is  $\sim 10$ – $20$ , but we cannot adopt a common value for all SNRs because the thermal components differ. This selection resulted in that 5 regions (subregions 4–8) in Kepler, 11 regions (subregions 3, 4, 6–9, 11–13, 17, and 20) in Tycho, and 12 region (subregions 1–6 and 10–15) in SN 1006 were synchrotron dominated, and the others are referred to as *thermal dominated*. We presumed that all the spectra in Cassiopeia A, RCW 86, and SN 1987A defined in this paper belonged to the synchrotron dominated group. It should be noted that the origin of a hard X-ray component in SN 1987A is unknown yet.

<sup>1</sup> Note that these synchrotron dominated remnants also have thermal components, particularly in the central regions.

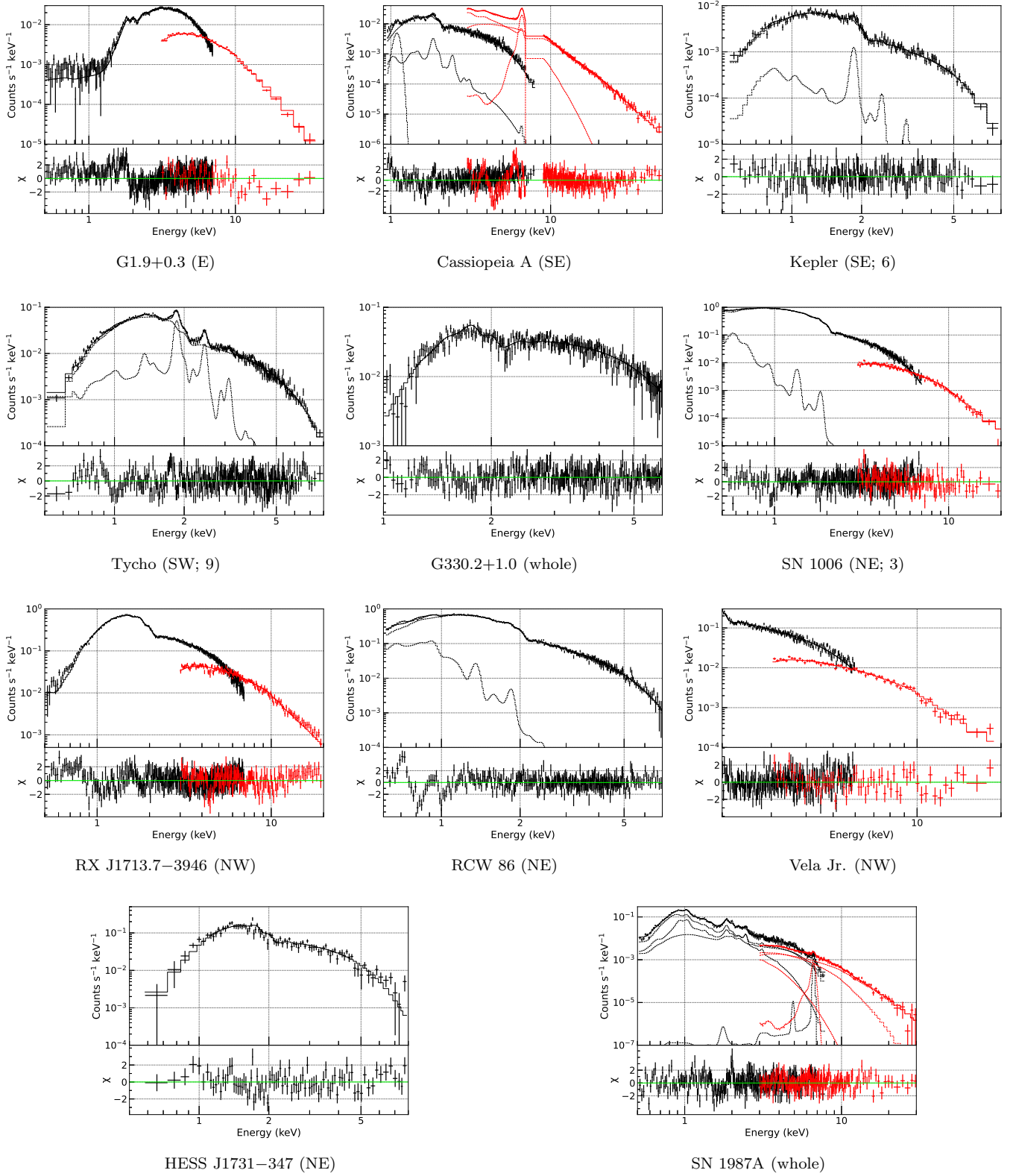


**Figure 2.** Spectrum of the representative region of each SNR with the best-fit model. The spectra extracted from the *Chandra* and *NuSTAR* data are respectively shown in black and red.

For those SNRs containing strong thermal components, we also fitted with only the ZA07 model, but using the spectra above 2.5 keV where the thermal components can be suppressed to some extent. We excluded the 6.4–6.8 keV channel if the spectrum has a sign of iron line emission. The cutoff energy parameter was roughly consistent between these two methods, although the one including the thermal model yielded slightly higher cutoff energy parameter. It should be noted that the thermal-dominated spectra defined above cannot be fitted only with the synchrotron model, resulting in large reduced chi-squared values of  $\chi^2_{\nu} \geq 2$ . We focus on the results of the synchrotron dominated spectra in this paper and leave, to the future publication, discussion of the relation between the thermal properties and the synchrotron radiation.

### 3.3.2. Acceleration efficiency

In the present framework, the cutoff energy parameter  $\varepsilon_0$  is a key factor characterizing shock acceleration in SNRs as it is determined by the balance between acceleration and synchrotron cooling. [Zirakashvili & Aharonian \(2007\)](#) derived a relation between the cutoff energy parameter and the shock velocity,

$$\varepsilon_0 = 1.6 \left( \frac{v_{\text{sh}}}{4000 \text{ km s}^{-1}} \right)^2 \eta^{-1} \text{ keV}. \quad (2)$$

Equation 2 yields a relation determining the Bohm factor:

$$\eta = 1.6 \left( \frac{v_{\text{sh}}}{4000 \text{ km s}^{-1}} \right)^2 \left( \frac{\varepsilon_0}{\text{keV}} \right)^{-1}. \quad (3)$$

Combining the measured cutoff energy parameter and the known shock speed, we can estimate the value of  $\eta$  using Equation 3. Table 2 lists the obtained  $\eta$  parameter as well as the shock velocity in each region of SNR analyzed in Section 3.2.

### 3.3.3. Validity of cooling-limited model

We need to test the validity of the models (Equation 1 and Equation 2) which are derived based on the assumption of the cooling-limited case, since acceleration in young SNRs can be limited by an age instead. In the synchrotron-cooling-limited case, the acceleration timescale ( $\tau_{\text{acc}}$ ) is comparable to the synchrotron-cooling timescale ( $\tau_{\text{synch}}$ ; defined as, e.g., Equation (23) in [Zirakashvili & Aharonian \(2007\)](#) for  $\kappa = \sqrt{11}^{-1}$ ) and is shorter than the characteristic dynamical timescale of the source, such as the age of the accelerator ( $\tau_{\text{age}}$ ). Therefore, to fulfill our assumption, the condition that follows should be satisfied for the energy of synchrotron-emitting electrons:

$$\tau_{\text{acc}} \approx \tau_{\text{synch}} \leq \tau_{\text{age}}. \quad (4)$$

We can place a lower limit value on the magnetic field by imposing the condition of  $\tau_{\text{synch}} \leq \tau_{\text{age}}$ ,

$$B \geq B_{\text{low}} = 12 \left( \frac{t_{\text{age}}}{1 \text{ kyr}} \right)^{-\frac{2}{3}} \left( \frac{u_1}{4000 \text{ km s}^{-1}} \right)^{-\frac{2}{3}} \eta^{\frac{1}{3}} \mu\text{G}. \quad (5)$$

The lower limit of  $B$  calculated for each region is listed in Table 2.  $B_{\text{low}}$  was estimated to be 10–20  $\mu\text{G}$  in the galactic SNRs older than G330.2+1.0 with the age of at most a thousand years. This can be reasonably achieved given the magnetic field strength in the interstellar medium of  $\sim 4 \mu\text{G}$  and the standard shock compression of 4. For the younger SNRs, we obtained  $B_{\text{low}}$  of 30–40  $\mu\text{G}$ , which is still acceptable when considering magnetic field amplification. Indeed, it has been reported that the magnetic field strength is enhanced up to  $\sim 100 \mu\text{G}$ , inferred from the filament width (see, e.g., [Bamba et al. 2005](#); [Berezhko & Völk 2006](#)). An exceptionally high value of  $B_{\text{low}} = 170 \mu\text{G}$  was required for SN 1987A. It is worth noting that, for gamma-ray emitting SNRs,  $B_{\text{low}}$  derived from Equation 5 is compatible with or smaller than that obtained by modelling the with the leptonic () models in the literature.

**Table 2.** Nonthermal parameters and properties of particle acceleration (see also Table 6 for the parameters of the thermal model in Cassiopeia A, Kepler, Tycho, SN 1006, RCW 86, and SN 1987A).

Region	$N_H$ ( $10^{22} \text{ cm}^{-2}$ )	$\varepsilon_0$ (keV)	Flux <sup>(a)</sup>	$\chi^2$ (dof)	$v_{\text{sh}}$ <sup>(b)</sup> ( $\text{km s}^{-1}$ )	$m$ <sup>(c)</sup>	$\eta$	$B_{\text{low}}$ <sup>(d)</sup> ( $\mu\text{G}$ )
<b>G1.9+0.3</b>								
whole	$6 \pm 0.04$	$1.2 \pm 0.1$	$3.25^{+0.02}_{-0.04}$	902.2 (585)	$13000 \pm 1000$	$1.1 \pm 0.2$	$14.0 \pm 2.8$	$39 \pm 7$
N	$5.4 \pm 0.1$	$1.2 \pm 0.1$	$0.99^{+0.02}_{-0.01}$	697.3 (477)	$3600 \pm 500$	$0.4 \pm 0.2$	$1.1 \pm 0.4$	$39 \pm 9$
N-RS <sup>(e)</sup>	$5.4 \pm 0.1$	$1.2 \pm 0.1$	$0.99^{+0.02}_{-0.01}$	697.3 (477)	$5000 \pm 1000$	$0.4 \pm 0.2$	$2.2 \pm 1.0$	$39 \pm 10$
E	$6 \pm 0.1$	$1.4 \pm 0.1$	$2.02^{+0.03}_{-0.01}$	654.2 (492)	$13000 \pm 1000$	$1.1 \pm 0.2$	$12.1 \pm 2.6$	$37 \pm 7$
S	$5.7 \pm 0.1$	$0.9 \pm 0.1$	$0.77^{+0.02}_{-0.01}$	573.5 (479)	$3600 \pm 500$	$0.4 \pm 0.2$	$1.5 \pm 0.5$	$44 \pm 10$
S-RS <sup>(e)</sup>	$5.7 \pm 0.1$	$0.9 \pm 0.1$	$0.77^{+0.02}_{-0.01}$	573.5 (479)	$5000 \pm 1000$	$0.4 \pm 0.2$	$2.9 \pm 1.4$	$44 \pm 11$
W	$6.2 \pm 0.1$	$1.1 \pm 0.1$	$1.47^{+0.01}_{-0.02}$	641.5 (480)	$13000 \pm 1000$	$1.1 \pm 0.2$	$15.2 \pm 3.3$	$40 \pm 8$
<b>Cassiopeia A</b>								
N1	$1.16^{+0.02}_{-0.01}$	$0.54^{+0.03}_{-0.02}$	$27.1^{+0.3}_{-0.4}$	542 (398)	$4351 \pm 322$	$0.60 \pm 0.04$	$3.6 \pm 0.6$	$36 \pm 3$
N2	$1.06 \pm 0.02$	$0.44 \pm 0.03$	$10.4^{+0.1}_{-0.3}$	411 (338)	$4351 \pm 322$	$0.60 \pm 0.04$	$4.4 \pm 0.7$	$39 \pm 3$
S	$1.50^{+0.03}_{-0.04}$	$0.49 \pm 0.03$	$19.3^{+0.2}_{-0.4}$	512 (369)	$5479 \pm 483$	$0.75 \pm 0.07$	$6.3 \pm 1.2$	$37^{+4}_{-3}$
NW	$1.33 \pm 0.03$	$1.59^{+0.26}_{-0.18}$	$18.4^{+0.1}_{-1.0}$	375 (376)	$4512 \pm 483$	$0.62 \pm 0.07$	$1.3 \pm 0.3$	$25 \pm 3$
SE	$1.98 \pm 0.03$	$1.72 \pm 0.09$	$10.0^{+0.1}_{-0.2}$	1249 (661)	$5157 \pm 644$	$0.71 \pm 0.09$	$1.6 \pm 0.4$	$24 \pm 3$
E	$1.12 \pm 0.04$	$0.89^{+0.21}_{-0.15}$	$4.3^{+0.1}_{-0.4}$	310 (267)	$5157 \pm 322$	$0.65 \pm 0.04$	$3.1^{+0.8}_{-0.6}$	$30 \pm 3$
NE	$1.45 \pm 0.02$	$1.55 \pm 0.09$	$16.2 \pm 0.2$	896 (689)	$4835 \pm 483$	$0.67 \pm 0.07$	$1.5 \pm 0.3$	$25 \pm 3$
<b>Kepler</b>								
1	$0.38^{+0.02}_{-0.01}$	$1.54^{+1.73}_{-0.58}$	$1.08^{+0.04}_{-0.54}$	334 (170)	$2067 \pm 247$	$0.49 \pm 0.09$	$0.3^{+0.3}_{-0.1}$	$22^{+9}_{-4}$
2	$0.50 \pm 0.02$	$0.39^{+0.24}_{-0.12}$	$0.40^{+0.02}_{-0.28}$	273 (150)	$1972 \pm 284$	$0.47 \pm 0.10$	$1.0^{+0.7}_{-0.4}$	$35^{+9}_{-6}$
3	$0.41 \pm 0.02$	$0.76^{+0.19}_{-0.14}$	$1.51^{+0.04}_{-0.21}$	217 (178)	$2825 \pm 322$	$0.63 \pm 0.10$	$1.1^{+0.4}_{-0.3}$	$28^{+4}_{-3}$
4	$0.61^{+0.05}_{-0.02}$	$0.64^{+0.15}_{-0.09}$	$1.26^{+0.03}_{-0.14}$	143 (149)	$3622 \pm 284$	$0.68 \pm 0.08$	$2.1^{+0.6}_{-0.4}$	$29 \pm 3$
5	$0.64^{+0.05}_{-0.04}$	$0.49^{+0.08}_{-0.06}$	$1.51^{+0.04}_{-0.15}$	148 (164)	$3906 \pm 303$	$0.70 \pm 0.07$	$3.2^{+0.7}_{-0.6}$	$32 \pm 3$
6	$0.60 \pm 0.03$	$1.65^{+0.72}_{-0.41}$	$1.63^{+0.02}_{-0.34}$	170 (179)	$5727 \pm 910$	$0.98 \pm 0.17$	$2.0^{+1.1}_{-0.8}$	$21 \pm 4$
7	$0.51 \pm 0.03$	$0.53^{+0.12}_{-0.09}$	$0.92^{+0.03}_{-0.12}$	177 (142)	$3375 \pm 569$	$0.63 \pm 0.13$	$2.2^{+0.9}_{-0.8}$	$31^{+6}_{-5}$
8	$0.51^{+0.08}_{-0.06}$	$0.85^{+0.29}_{-0.19}$	$1.19^{+0.04}_{-0.19}$	176 (147)	$4589 \pm 474$	$0.82 \pm 0.09$	$2.5^{+1.0}_{-0.8}$	$27^{+4}_{-3}$
9	$0.46^{+0.03}_{-0.02}$	$0.80^{+0.24}_{-0.18}$	$1.13^{+0.03}_{-0.22}$	227 (154)	$3906 \pm 398$	$0.71 \pm 0.09$	$1.9^{+0.7}_{-0.6}$	$27^{+4}_{-3}$
10	$0.36 \pm 0.04$	$1.94^{+4.32}_{-0.88}$	$0.56^{+0.01}_{-0.55}$	215 (126)	$3072 \pm 417$	$0.55 \pm 0.10$	$0.5^{+1.1}_{-0.3}$	$20^{+15}_{-4}$
11	$0.49^{+0.05}_{-0.04}$	$1.14^{+1.62}_{-0.48}$	$0.34^{+0.005}_{-0.281}$	96 (92)	$4020 \pm 759$	$0.72 \pm 0.15$	$1.4^{+2.1}_{-0.8}$	$24^{+12}_{-6}$
12	$0.65^{+0.09}_{-0.10}$	$1.06^{+0.72}_{-0.33}$	$0.59^{+0.01}_{-0.31}$	178 (119)	$3413 \pm 512$	$0.62 \pm 0.11$	$1.1^{+0.8}_{-0.5}$	$25^{+7}_{-4}$
13	$0.54 \pm 0.02$	$1.53^{+2.61}_{-0.64}$	$1.27^{+0.03}_{-1.18}$	456 (177)	$1441 \pm 607$	$0.34 \pm 0.16$	$0.1^{+0.3}_{-0.1}$	$22^{+15}_{-9}$
14	$0.12 \pm 0.04$	$0.42^{+0.16}_{-0.10}$	$1.00^{+0.03}_{-0.28}$	314 (171)	$2162 \pm 266$	$0.50 \pm 0.09$	$1.1^{+0.5}_{-0.4}$	$34^{+6}_{-5}$
<b>Tycho</b>								
1	$0.89 \pm 0.04$	$0.24 \pm 0.02$	$5.5^{+0.2}_{-0.3}$	484 (283)	$2380 \pm 238$	$0.37 \pm 0.04$	$2.5 \pm 0.5$	$40 \pm 4$
2	$0.77 \pm 0.04$	$0.18 \pm 0.01$	$9.8^{+0.2}_{-0.3}$	401 (301)	$3000 \pm 500$	$0.51 \pm 0.08$	$5.0 \pm 1.7$	$43 \pm 7$
3	$0.59 \pm 0.03$	$0.33 \pm 0.01$	$23.8 \pm 0.4$	518 (369)	$3200 \pm 320$	$0.55 \pm 0.05$	$3.2 \pm 0.6$	$35 \pm 3$
4	$0.66 \pm 0.01$	$0.38 \pm 0.01$	$29.8^{+0.3}_{-0.4}$	561 (399)	$3580 \pm 358$	$0.56 \pm 0.06$	$3.4 \pm 0.7$	$34 \pm 3$
5	$0.91 \pm 0.04$	$0.40 \pm 0.02$	$30.5^{+0.3}_{-0.6}$	717 (404)	$3700 \pm 370$	$0.58 \pm 0.06$	$3.5 \pm 0.7$	$33 \pm 3$
6	$0.76^{+0.05}_{-0.04}$	$0.42^{+0.03}_{-0.02}$	$26.3^{+0.3}_{-0.6}$	640 (396)	$3850 \pm 385$	$0.60 \pm 0.06$	$3.6 \pm 0.8$	$33 \pm 3$

**Table 2** continued on next page



**Table 2** (*continued*)

Region	$N_H$ ( $10^{22} \text{ cm}^{-2}$ )	$\varepsilon_0$ (keV)	Flux <sup>(a)</sup>	$\chi^2$ (dof)	$v_{\text{sh}}$ <sup>(b)</sup> ( $\text{km s}^{-1}$ )	$m$ <sup>(c)</sup>	$\eta$	$B_{\text{low}}$ <sup>(d)</sup> ( $\mu\text{G}$ )
7	$0.77 \pm 0.01$	$0.36 \pm 0.01$	$26.4^{+0.3}_{-0.5}$	605 (396)	$3920 \pm 648$	$0.61 \pm 0.10$	$4.3 \pm 1.4$	$34 \pm 5$
8	$0.78^{+0.02}_{-0.01}$	$0.39 \pm 0.02$	$20.4^{+0.3}_{-0.5}$	419 (363)	$3980 \pm 418$	$0.62 \pm 0.07$	$4.1 \pm 0.9$	$33 \pm 3$
9	$0.81 \pm 0.02$	$0.55^{+0.04}_{-0.03}$	$16.9^{+0.2}_{-0.4}$	486 (366)	$4060 \pm 634$	$0.63 \pm 0.10$	$3.1 \pm 1.0$	$30 \pm 4$
10	$1.16 \pm 0.06$	$0.35 \pm 0.03$	$11.8^{+0.2}_{-0.3}$	651 (335)	$3780 \pm 378$	$0.59 \pm 0.06$	$4.2 \pm 0.9$	$35 \pm 3$
11	$0.74 \pm 0.03$	$0.41^{+0.03}_{-0.02}$	$17.7^{+0.2}_{-0.4}$	427 (371)	$3240 \pm 468$	$0.54 \pm 0.07$	$2.6 \pm 0.8$	$33 \pm 5$
12	$0.64^{+0.05}_{-0.04}$	$0.42 \pm 0.03$	$14.9^{+0.2}_{-0.5}$	536 (360)	$3480 \pm 538$	$0.59 \pm 0.08$	$3.0 \pm 0.9$	$33 \pm 5$
13	$0.74 \pm 0.03$	$0.40^{+0.04}_{-0.03}$	$9.2^{+0.2}_{-0.5}$	452 (308)	$3330 \pm 333$	$0.57 \pm 0.05$	$2.8 \pm 0.6$	$33 \pm 3$
14	$1.09 \pm 0.04$	$0.40 \pm 0.04$	$12.8^{+0.2}_{-0.4}$	601 (351)	$3510 \pm 351$	$0.55 \pm 0.05$	$3.1 \pm 0.7$	$33 \pm 3$
15	$0.55 \pm 0.03$	$0.44 \pm 0.03$	$12.0^{+0.2}_{-0.5}$	458 (344)	$3110 \pm 311$	$0.49 \pm 0.05$	$2.2 \pm 0.5$	$32 \pm 3$
16	$0.73 \pm 0.03$	$0.41^{+0.03}_{-0.02}$	$11.9^{+0.2}_{-0.4}$	601 (329)	$2210 \pm 378$	$0.38 \pm 0.06$	$1.2 \pm 0.4$	$33 \pm 5$
17	$0.65 \pm 0.02$	$0.57 \pm 0.02$	$56.6^{+0.4}_{-0.6}$	810 (428)	$2000 \pm 400$	$0.36 \pm 0.06$	$0.7 \pm 0.3$	$30 \pm 6$
18	$1.10^{+0.14}_{-0.06}$	$0.28 \pm 0.02$	$12.5^{+0.2}_{-0.4}$	664 (341)	$2360 \pm 236$	$0.39 \pm 0.04$	$2.1 \pm 0.4$	$37 \pm 4$
19	$0.80 \pm 0.02$	$0.41 \pm 0.02$	$17.5^{+0.2}_{-0.4}$	583 (371)	$3310 \pm 331$	$0.52 \pm 0.05$	$2.7 \pm 0.6$	$33 \pm 3$
20	$0.58 \pm 0.02$	$0.38 \pm 0.02$	$17.1^{+0.2}_{-0.3}$	530 (372)	$3660 \pm 366$	$0.57 \pm 0.06$	$3.6 \pm 0.7$	$34 \pm 3$
G330.2+1.0								
whole	2.5 (fixed)	$1.17^{+0.32}_{-0.22}$	$2.52^{+0.39}_{-0.03}$	244.6 (269)	$7000 \pm 2000$	$0.9 \pm 0.3$	$4.3^{+2.7}_{-2.6}$	$17 \pm 7$
SN 1006								
1	$0.13 \pm 0.02$	$0.15 \pm 0.01$	$6.3^{+0.3}_{-0.6}$	292 (279)	$6500 \pm 500$	$0.75 \pm 0.06$	$28.6 \pm 4.7$	$26 \pm 2$
2	$0.11 \pm 0.01$	$0.37 \pm 0.01$	$75 \pm 1$	609 (505)	$5900 \pm 500$	$0.68 \pm 0.06$	$9.6 \pm 1.6$	$20 \pm 2$
3	$0.10 \pm 0.01$	$0.50 \pm 0.02$	$88 \pm 1$	566 (525)	$5500 \pm 800$	$0.64 \pm 0.09$	$6.2 \pm 1.8$	$18 \pm 2$
4	$0.09 \pm 0.01$	$0.37^{+0.02}_{-0.01}$	$65^{+1}_{-2}$	555 (431)	$5000 \pm 500$	$0.64 \pm 0.06$	$6.9 \pm 1.4$	$20 \pm 2$
5	$0.12 \pm 0.01$	$0.31 \pm 0.02$	$17^{+0}_{-1}$	290 (277)	$4900 \pm 500$	$0.62 \pm 0.06$	$8.0 \pm 1.7$	$21 \pm 2$
6	$0.09 \pm 0.01$	$0.20 \pm 0.01$	$21 \pm 1$	403 (318)	$5800 \pm 500$	$0.74 \pm 0.06$	$17.2 \pm 3.1$	$24 \pm 2$
7	0.11	$0.13^{+0.03}_{-0.04}$	$1.3^{+0.3}_{-0.7}$	325 (171)	$7000 \pm 1200$	$0.89 \pm 0.15$	$37.4^{+16.1}_{-16.4}$	$27 \pm 5$
8	0.11	$0.56^{+0.56}_{-0.23}$	$5.6^{+0.3}_{-4.2}$	233 (179)	$7200 \pm 1000$	$0.92 \pm 0.13$	$9.5^{+9.9}_{-4.7}$	$17^{+6}_{-3}$
9	$0.14^{+0.05}_{-0.04}$	$0.09 \pm 0.01$	$2.3^{+0.3}_{-0.4}$	295 (202)	$5000 \pm 800$	$0.64 \pm 0.10$	$27.4^{+9.2}_{-9.1}$	$31 \pm 5$
10	$0.15 \pm 0.02$	$0.20 \pm 0.01$	$27 \pm 1$	327 (319)	$5000 \pm 800$	$0.64 \pm 0.10$	$12.5 \pm 4.1$	$24 \pm 4$
11	$0.14 \pm 0.01$	$0.30 \pm 0.01$	$60 \pm 1$	574 (414)	$5500 \pm 500$	$0.70 \pm 0.06$	$10.4^{+2.0}_{-1.9}$	$21 \pm 2$
12	$0.11 \pm 0.01$	$0.31 \pm 0.01$	$48 \pm 1$	498 (457)	$5900 \pm 800$	$0.75 \pm 0.10$	$11.4 \pm 3.1$	$21 \pm 3$
13	$0.10^{+0.02}_{-0.01}$	$0.32 \pm 0.02$	$37 \pm 1$	439 (352)	$7500 \pm 400$	$0.96 \pm 0.05$	$18.0 \pm 2.2$	$21 \pm 1$
14	$0.12 \pm 0.02$	$0.23 \pm 0.02$	$10.3^{+0.4}_{-0.9}$	216 (228)	$5500 \pm 500$	$0.70 \pm 0.06$	$13.6 \pm 2.7$	$23 \pm 2$
15	$0.01^{+0.04}_{-0.01}$	$0.17^{+0.01}_{-0.02}$	$2.3^{+0.2}_{-0.5}$	223 (197)	$7000 \pm 1000$	$0.89 \pm 0.13$	$28.8^{+8.5}_{-9.1}$	$25^{+3}_{-4}$
16	$0.23^{+0.05}_{-0.03}$	$0.03^{+0.02}_{-0.01}$	$0.04^{+0.01}_{-0.03}$	283 (184)	$3000 \pm 1200$	$0.44 \pm 0.18$	$31.4^{+30.7}_{-28.2}$	$46^{+19}_{-18}$
17	0.12	$0.03^{+0.02}_{-0.01}$	$0.53^{+0.06}_{-0.49}$	173 (122)	$3000 \pm 1200$	$0.38 \pm 0.15$	$27.8^{+27.3}_{-23.2}$	$44^{+18}_{-17}$
RX J1713.7–3946								
NW	$0.75 \pm 0.01$	$1.14 \pm 0.06$	$11.5^{+0.3}_{-0.2}$	687.9 (587)	$3900 \pm 300$	$0.7 \pm 0.1$	$1.4 \pm 0.3$	$9.7 \pm 0.9$
RCW 86								
NE	0.33 (fixed)	$0.32 \pm 0.01$	$3.22^{+0.03}_{-0.05}$	527 (407)	$2500 \pm 700$	$0.3 \pm 0.1$	$2.0 \pm 1.1$	$14 \pm 4$
Vela Jr.								
NW	0.67 (fixed)	$0.54 \pm 0.04$	$3.9 \pm 0.1$	289.3 (258)	$2000 \pm 600$	$0.5 \pm 0.2$	$0.7 \pm 0.5$	$8^{+3}_{-4}$

**Table 2** *continued on next page*

Table 2 (*continued*)

Region	$N_H$ ( $10^{22} \text{ cm}^{-2}$ )	$\varepsilon_0$ (keV)	Flux <sup>(a)</sup>	$\chi^2$ (dof)	$v_{\text{sh}}$ <sup>(b)</sup> ( $\text{km s}^{-1}$ )	$m$ <sup>(c)</sup>	$\eta$	$B_{\text{low}}$ <sup>(d)</sup> ( $\mu\text{G}$ )
HESS J1731–347								
NE	1 (fixed)	$0.97^{+0.46}_{-0.26}$	$3.6^{+1.2}_{-0.1}$	102.7 (86)	$2500 \pm 1000$	$0.5 \pm 0.1$	$0.65^{+0.61}_{-0.55}$	$6^{+3}_{-12}$
SN 1987A								
whole	$0.18 \pm 0.02$	$0.70^{+0.36}_{-0.08}$	$2.49^{+0.07}_{-0.02}$	610.7 (497)	$6700 \pm 800$	$0.9 \pm 0.1$	$6.5 \pm 2.6$	$165^{+16}_{-17}$
whole-RS <sup>(e)</sup>	$0.18 \pm 0.02$	$0.70^{+0.36}_{-0.08}$	$2.49^{+0.07}_{-0.02}$	610.7 (497)	$4800 \pm 300$	$0.9 \pm 0.1$	$3.4 \pm 1.0$	$165^{+11}_{-13}$

NOTE— (a) Flux is calculated for the 4–6 keV band in Cassiopeia A, Kepler, Tycho, and SN 1006 in units of  $10^{-14} \text{ erg cm}^{-2} \text{ s}^{-1}$ , while is for the 2–10 keV band in the other SNRs in units of  $10^{-12} \text{ erg cm}^{-2} \text{ s}^{-1}$ .

(b) References (see also Table 1). G1.9+0.3: Borkowski et al. (2017). Cassiopeia A: Patnaude & Fesen (2009). Kepler: Vink (2008); Katsuda et al. (2008b). Tycho: Katsuda et al. (2010a); Williams et al. (2013). G330.2+1.0: Borkowski et al. (2018). SN 1006: Winkler et al. (2014). RX J1713.7–3946: Tsuji & Uchiyama (2016); Acero et al. (2017). RCW 86: Yamaguchi et al. (2016). Vela Jr.: Katsuda et al. (2008a); Allen et al. (2015). HESS J1731–347: H. E. S. S. Collaboration et al. (2011). SN 1987A: Frank et al. (2016).

(c) Expansion parameter.

(d) Lower limit of magnetic field required for cooling-limited assumption (Equation 5).

(e) RS: Assuming the reverse shock or reflection shock.

## 4. RESULTS

### 4.1. Relation between shock speed and cutoff energy

In this section we study the possible correlation between the cutoff energy from our analysis in Section 3.3 and the shock speed taken from the literature (see references in Tables 1 and 2). Our results show that there is a significant variance of both the cutoff energy parameter and the shock velocity in the considered SNR (see in Figure 3). Below we discuss the result for each SNR, and in Section 4.2 we consider the source averaged acceleration efficiencies. We also show in Figure 3 (top left panel) a compilation of the largest- $\varepsilon_0$  region of each SNR, which is highlighted by the thick line in Figure 1 and nearly corresponds to the maximum shock-speed region. In this maximum- $\varepsilon_0$  region, the acceleration is the most efficient, and the result is discussed in Section 4.2 and Section 5.2.

In Figure 3, we also show the obtained  $v_{\text{sh}}-\varepsilon_0$  relation of G1.9+0.3, Cassiopeia A, Kepler, Tycho, and SN 1006. For Kepler, Tycho, and SN 1006, we separately showed the thermal dominated and nonthermal (synchrotron) dominated spectra (see Section 3.3.1). As mentioned in Section 3.3.1, in the thermal dominated spectrum the cutoff energy might not be appropriate because the spectrum in the higher energy range, fitted by the ZA07 model, may not be of synchrotron radiation origin, but Bremsstrahlung or hotter thermal plasma. Furthermore, the proper motion in the thermal-dominated regions might represent the speed of ejecta components rather than blast waves. Hence, our objective to examine acceleration efficiency cannot be achieved in these thermal regions (i.e., both cutoff energy and shock speed would not be robust in terms of particle acceleration). There exist variations of the shock speed and cutoff energy across the remnants in Figure 3, and the summary will be given in Section 5.1. Note that the spatially resolved  $v_{\text{sh}}-\varepsilon_0$  plots can be obtained only in these five SNRs, since the shock velocity was not measured across the remnant in the other SNRs<sup>2</sup>. In addition to them, the  $v_{\text{sh}}-\varepsilon_0$  relation in the north west rim of RX J1713.7–3946 was already provided in details in Tsuji et al. (2019). We make a brief description of the nature of particle acceleration of individual SNRs in the following and present a systematical tendency of particle acceleration of young SNRs in Section 4.2.

#### 4.1.1. G1.9+0.3

<sup>2</sup> The proper motion was measured to be different from region to region in G330.2+1.0, as reported in Williams et al. (2018), but due to its faint radiation we could not obtain the spatially resolved cutoff energy. In RCW 86, proper motion measurement with X-ray observations was conducted in the northeast rims (Yamaguchi et al. 2016), while proper motion with optical observations was measured in the other regions. However X-ray and optical measurements were different by a factor of about 2. We made use of the shock speed measured with X-rays since accelerated electrons are traced by the synchrotron X-ray emission.

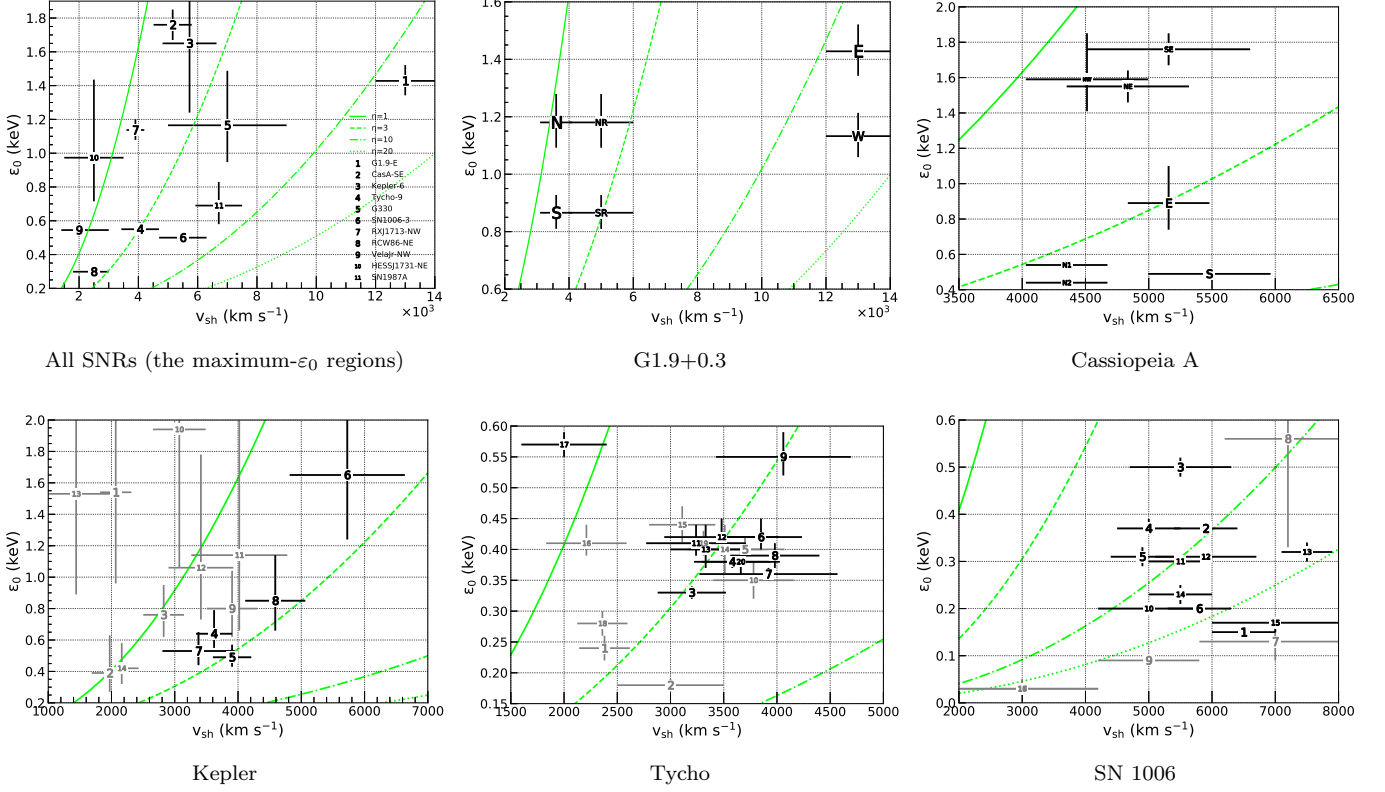


**Figure 3.**  $\varepsilon_0$ - $v_{\text{sh}}$  diagram. Green solid, dashed, dash-dotted, and dotted lines indicate  $\eta$  of 1, 3, 10, and 20, respectively. Top left: Each plot is taken from the region having the largest  $\varepsilon_0$  (or the maximum  $v_{\text{sh}}$ ) in each SNR, where the region is highlighted in Figure 1. For Kepler, Tycho, and SN 1006, results of the synchrotron-dominated regions are shown in black, while those of the thermal-dominated regions are shown in grey (see Section 3.3.1). In G1.9+0.3, NR and SR indicate the results assuming that the emission originates from the reverse shock in the north and south regions, respectively.

G1.9+0.3, known as the youngest SNR in our galaxy, showed that the cutoff energy parameters were slightly variable inside the remnant:  $\varepsilon_0$  was obtained to be 1.1–1.2 keV in the entire remnant, the western and northern regions, whereas it was slightly higher in the eastern rim ( $\varepsilon_0 \approx 1.4$  keV) and lower in the southern part ( $\varepsilon_0 \approx 0.9$  keV). It should be noted that these differences in the measured cutoff energy parameters may have been underestimated because of the overlapped subregions and the limited angular resolution of *NuSTAR*. In the case of forward shock, the Bohm factor was estimated to be 12–15 in the bright rim of E and W with the faster shock velocity of  $\sim 13000$  km s $^{-1}$ . This was roughly consistent with  $\eta \sim 20$  obtained in [Aharonian et al. \(2017\)](#). However,  $\eta$  was 1–2 in the fainter area of N and S, with the slower shock speed of  $\sim 4000$  km s $^{-1}$ . The  $\eta$  parameter averaged over the entire remnant (the N, E, S, and W regions) was  $7.5 \pm 0.8$ . If we assume the outward proper motions in the N and S rims, which were measured in [Borkowski et al. \(2017\)](#), correspond to the reverse shock, the upstream speed in the rest frame of the reverse shock is given by

$$u_1 = \frac{R_{\text{ref}}}{t_{\text{age}}} - v_{\text{obs}} \quad (6)$$

([Sato et al. 2018](#); [Tsuji et al. 2019](#)). Indeed the reverse shock might play a major role in the northern region where the radio synchrotron emission is strong, and the proper motion of the shock is reduced, as proposed in ([Brose et al. 2019](#)). Using Equation 6,  $u_1$  in N and S is approximately calculated to be 5000 km s $^{-1}$ , resulting in  $\eta \sim 2$ –3. We apparently see a significant difference in the acceleration efficiency across the remnant: the Bohm factor in the bright E–W rim is approximately one order of magnitude higher than that in the N–S part in the case of either the forward shock or reverse shock.

#### 4.1.2. Cassiopeia A

The seven sectors (N1–2, NE, E, SE, S, and NW) are roughly compatible with the regions which Patnaude & Fesen (2009) measured proper motions and showed that the speeds are almost constant of  $\sim 5000 \text{ km s}^{-1}$ , assuming a distance of 3.4 kpc. The cutoff energy parameters indicate significant varieties, showing the highest value in the SE rim and the lowest value in the N2 region. Because of the constant shock speeds and different cutoff energy parameters, the  $\eta$  values also varied from 1.5 in SE and 6.3 in S. This trend was consistent with the previous result in Stage et al. (2006). In the case of the forward shock in Cassiopeia A, the variation of  $\eta$  is attributed to the different values of  $\varepsilon_0$ , which is opposite to G1.9+0.3 showing the variable shock speed and roughly constant  $\varepsilon_0$ . If we averaged the  $\eta$  parameters obtained in the seven small regions, the averaged  $\eta$  was derived to be  $3.1 \pm 0.3$ .

#### 4.1.3. Kepler's SNR

We defined 14 subregions that are almost comparable to those defined by Katsuda et al. (2008b), who performed proper motion measurements. Five of these subregions (labeled as 4–8) turned out to be synchrotron dominated and highlighted in Figure 3. The observed  $v_{\text{sh}}-\varepsilon_0$  relation of these five regions indicated a clear correlation of  $\varepsilon_0$  and  $v_{\text{sh}}$  (i.e., the higher the shock speed is, the larger the cutoff energy parameter is). In addition, the correlation is well described with the theoretical curve with  $\eta$  of 2–3. This clarifies that the acceleration efficiency is constant ( $\eta=2-3$ ) and independent of the sites within the forward shock located in the outermost eastern and southern rims of Kepler. The averaged  $\eta$  over the 5 synchrotron dominated regions was  $2.4^{+0.3}_{-0.4}$ . Our analysis, for the first time, found that the particle acceleration in Kepler at the evolutionary age of  $\sim 400$  years significantly deviates from the maximum rate of  $\eta = 1$ .

#### 4.1.4. Tycho's SNR

Figure 3 presents the  $v_{\text{sh}}-\varepsilon_0$  scatter plot measured in Tycho, in which 11 regions (subregions 3, 4, 6–9, 11–13, 17, and 20) are synchrotron dominated. Tycho shows slightly variable but theoretical predicted plots with  $\varepsilon_0 = 0.3-0.6$  keV and  $v_{\text{sh}} = 3000-4000 \text{ km s}^{-1}$  (Katsuda et al. 2010a; Williams et al. 2013). This corresponds to nearly constant acceleration efficiency with  $\eta$  of 3–4 (and the average value of  $3.1 \pm 0.3$ ) in the forward shock of Tycho. One exceptional region is subregion 17 located in the eastern rim. The  $\eta$  value should be  $\sim 1$  on the subregion 17, inferred from a slow shock speed of  $2000 \text{ km s}^{-1}$  and a higher cutoff energy parameter of 0.57 keV. This nonthermal radiation in the E rim might be unique and behave differently from the other parts because a precursor has been detected (Lee et al. 2010), and a dense clump known as *knot g* is present (see, for example, Ghavamian et al. (2000)). The dense density might affect the lower shock velocity of *knot g*. Note that our result was roughly consistent with that of Lopez et al. (2015), although the model and region definition were different (i.e., they also showed the greater roll-off energies in the higher shock speeds and the exception of *knot g*).

#### 4.1.5. SN 1006

The filaments in the NE and SW limbs were dominated by synchrotron emission. Thus, the spectra of the subregions 2–4 (NE) and 11–13 (SW), extracted both with *Chandra* and *NuSTAR*, represent the typical properties of the synchrotron radiation from this remnant. They showed somewhat small cutoff energy parameters ( $\varepsilon_0 = 0.3-0.4$  keV) and relatively high shock speeds ( $v_{\text{sh}} = 5000-8000 \text{ km s}^{-1}$ ), suggesting inefficient particle acceleration ( $\eta \sim 10$ ) in SN 1006. Note that the cutoff energy parameters obtained in this paper were roughly consistent with those of Li et al. (2018). The other subregions (1, 5–10, and 14–17) were analyzed using only *Chandra*, as *NuSTAR* covered only two limbs in the NE and SW parts. The synchrotron dominated regions (1–6 and 10–15) showed a clear variation in  $\varepsilon_0$  but a nearly constant value in  $v_{\text{sh}}$ . The averaged  $\eta$  parameter over the synchrotron dominated spectra was  $14 \pm 1$ .

The validity of the loss-limited assumption is controversial in SN 1006. Katsuda et al. (2010b) suggested that the accelerated electrons may not be loss-limited, while Miceli et al. (2013) found evidence supporting the loss limited scenario. In this work, we obtained  $B$  should be larger than  $20-30 \text{ } \mu\text{G}$  for the ZA07 model to be applicable to SN 1006. This condition can be sufficiently fulfilled, adopting  $B \sim 300 \text{ } \mu\text{G}$  that was estimated by the filament width (Bamba et al. 2003; Völk et al. 2005).

We also investigated a shock-obliquity dependency on particle acceleration in SN 1006. SN 1006 is a unique remnant of which the ambient magnetic field was reported to be along the galactic plane that is approximately  $60^\circ$  counterclockwise inclined from the north (see, e.g., Reynoso et al. 2013). This oriented magnetic field, combined with the Type Ia explosion in a high Galactic latitude of  $14.6^\circ$ , makes SN 1006 an ideal laboratory for studying the dependence of particle acceleration on magnetic field configurations (i.e., *parallel* or *perpendicular* shocks). The azimuthal variations of roll-off frequencies (with the SRCUT model in XSPEC) and shock velocities were studied in Rothenflug et al. (2004);

Miceli et al. (2009); Winkler et al. (2014). Our measurements of  $\varepsilon_0$  indicated the larger cutoff energy parameters near the polar regions (NE and SW), which is consistent with the previous studies. The observed variations of  $\varepsilon_0$  and  $v_{\text{sh}}$  enabled us to reproduce a clear correlation between the shock obliquity  $\theta_{\text{Bn}}$  and acceleration efficiency  $\eta$  in the synchrotron dominated regions, as illustrated in Figure 4. It should be noted that in NW and SE (subregions 7–9 and 16–17), where  $\theta_{\text{Bn}}$  is close to  $90^\circ$ , the thermal emission dominates and the proper motion there is representative of X-ray emitting ejecta knots, not shock waves. The shock-obliquity dependence on particle acceleration is discussed in Section 5.

#### 4.1.6. SN 1987A

Although the soft X-ray spectrum of SN 1987A below  $\sim 7$  keV is well-fitted by a thermal model of two-temperature plasmas (i.e., Vpshock and Vequil in XSPEC), there exists an apparent excess in the *NuSTAR* spectrum above 10 keV, which cannot not be described by the thermal model. The origin of the hard X-ray emission with *NuSTAR* remains unclear (Boggs et al. 2015; Reynolds et al. 2015). Malyshev et al. (2019) recently reported GeV emission detected with *Fermi* likely from SN 1987A. Presuming that this GeV radiation originates from SN 1987A, there should be a population of nonthermal particles, and thus its synchrotron emission could be considered as a plausible interpretation of the hard X-ray excess. In this paper, we simply assumed that the hard component of *NuSTAR* is described by the nonthermal (synchrotron) radiation, resulting in  $\varepsilon_0 \approx 0.7$  keV.

The expansion velocity of SN 1987A was reduced from  $\sim 7000$  km s $^{-1}$  to  $\sim 1000$  km s $^{-1}$  when impacting with the equatorial ring around 2003. We are interested in the shock velocity which is relevant for the acceleration of the X-ray emitting particles, thus adopted the former value (before the impact) for the shock speed of SN 1987A. The following two factors should be addressed: (i) X-ray emitting particles cannot be accelerated if the shock speed is as slow as 1000 km s $^{-1}$ . (ii) The cooling time of TeV electrons even in a strong magnetic field of  $B \sim 300$   $\mu$ G exceeds significantly 10 years,  $t_{\text{syn}} = 140$  yr  $(E/1 \text{ TeV})^{-1} (B/300 \mu\text{G})^{-2}$ . Therefore, in the framework on the adopted stationary approach model by Zirakashvili & Aharonian (2007), we should use the shock velocity relevant to the moment of TeV particle acceleration (i.e., we chose  $v_{\text{sh}} \approx 7000$  km s $^{-1}$ ). Combined with the cutoff energy parameter, the Bohm factor was estimated to be  $\sim 7$ . The detailed discussion of particle acceleration in SN 1987A will be given in the future publication.

#### 4.1.7. Others

We could not investigate the spatially resolved  $\varepsilon_0$ – $v_{\text{sh}}$  relation in the other SNRs (i.e., G330.2+1.0, RX J1713.7–3946, RCW 86, Vela Jr., HESS J1731–347, and SN 1987A) due to lacking observational data. The proper motions were measured along the rim of G330.2+1.0 (Borkowski et al. 2018), but due to the large uncertainty of the shock speed and the cutoff energy parameter the spatially resolved  $\varepsilon_0$ – $v_{\text{sh}}$  plot was not presented in this paper. The  $\varepsilon_0$ – $v_{\text{sh}}$  diagram of the NW rim in RX J1713.7–3946 was presented in Tsuji et al. (2019). To date the shock speeds were obtained only in specific regions, the NE rim in RCW 86 and the NW rim in Vela Jr., since these two SNRs have relatively large angular sizes of  $\sim 0.7^\circ$  and  $\sim 2^\circ$ , respectively.

### 4.2. Systematic tendency of $\eta$

We obtained the  $\eta$  values that are indicative of acceleration efficiency (Bohm factor) in the 11 individual SNRs. This subsection presents the systematic trend of  $\eta$  when all these SNRs are considered together. Because five SNRs showed significantly different properties of particle acceleration depending on the sites (Section 4.1), we investigated the systematical  $\eta$  values estimated from the selected regions based on the largest- $\varepsilon_0$  regions in Section 4.2.1. We also present the results using the  $\eta$  values averaged over the remnants. Section 4.2.2 presents the result of different supernova explosion types.

#### 4.2.1. Largest- $\varepsilon_0$ (maximum- $v_{\text{sh}}$ ) region

We investigated acceleration efficiency ( $\eta$ ) obtained in the region with the largest  $\varepsilon_0$  of each SNR. Note that the largest- $\varepsilon_0$  region nearly corresponded to the fastest- $v_{\text{sh}}$  region, except for SN 1006, which showed a slightly inverse correlation between  $\varepsilon_0$  and  $v_{\text{sh}}$ . Figure 5 (left) illustrates the relation between the estimated  $\eta$  value and the age of each SNR. We confirmed a tendency in which  $\eta$  decreased as the age of SNR increased. In SNRs younger than a few 100 years, the acceleration efficiency substantially deviated from the Bohm limit (i.e.,  $\eta > 1$ ). In the later evolutionary stage older than a few 1,000 years, the acceleration proceeded at the most efficient rate (i.e., Bohm limit with  $\eta \approx 1$ ).



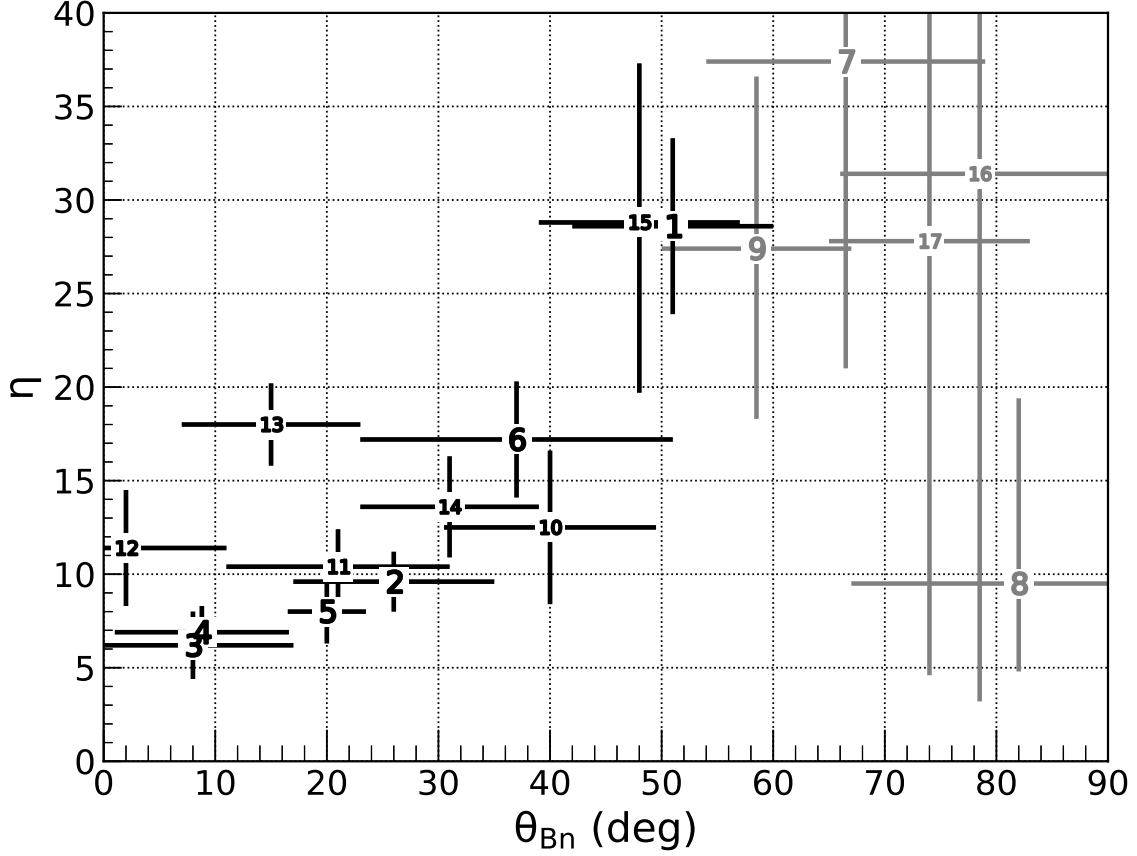


**Figure 4.** The  $\eta$  variation in SN 1006 as a function of shock obliquity, assuming the shock inclination is  $60^\circ$  from the north. The black and grey plots show the synchrotron dominated and thermal dominated regions, respectively.

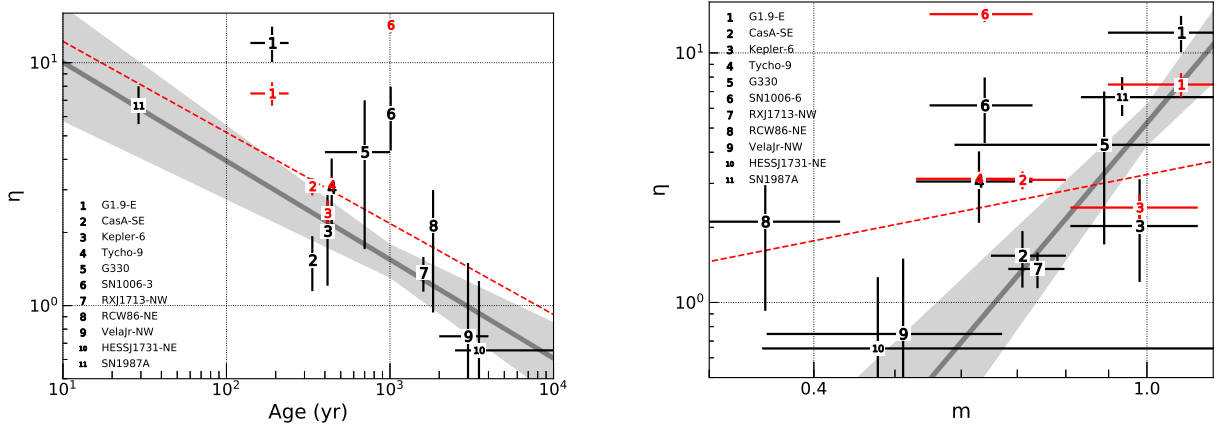


**Figure 5.**  $\eta$  as a function of the age (left) and expansion parameter  $m$  (right). The  $\eta$  parameters averaged over the synchrotron dominated regions are shown in red, and the model fitted with the averaged values is shown with the red dashed line.

To quantify the relation between  $\eta$  and  $t_{\text{age}}$ , we fit the observed diagram using an empirical equation,

$$\eta = C_{\text{age}} \left( \frac{t_{\text{age}}}{1 \text{ kyr}} \right)^{-\delta_{\text{age}}}, \quad (7)$$

where  $C_{\text{age}}$  and  $\delta_{\text{age}}$  indicate a constant value of  $\eta$  at the age of 1 kyr and a slope of the age- $\eta$  relation, respectively. With chi-squared fitting, we obtained  $C_{\text{age}} = 1.5 \pm 0.2$  and  $\delta_{\text{age}} = 0.41 \pm 0.08$ . A correlation coefficient of the logarithm-scale plots in Figure 5 (left) was approximately  $-0.70$  with a significance of  $2.4\sigma$ . The best-fit model is indicated by the grey line, and the 90% uncertainty is indicated by the light grey region in Figure 5. The best-fit parameters are summarized in Table 3. When we considered the averaged  $\eta$  instead of the largest- $\varepsilon_0$  region for G1.9+0.3, Cassiopeia A, Kelper, Tycho, and SN 1006,  $C_{\text{age}}$  and  $\delta_{\text{age}}$  were  $2.2 \pm 0.2$  and  $0.37 \pm 0.06$ , respectively, and a correlation coefficient was  $-0.65$  with a significance of  $2.2\sigma$ . Equation 7 nicely reproduces the observation, although G1.9+0.3 and SN 1006 significantly deviate from the best-fit model. The deviations in the two SNRs might arise from the fact that they are limited by some different factors, such as magnetic field or age, instead of cooling. If we omitted the results of G1.9+0.3 and SN 1006, the correlation coefficient was obtained to be  $-0.81$  with  $2.7\sigma$  ( $-0.89$  with  $3.0\sigma$  using the averaged  $\eta$ ).

Figure 5 (right) indicates the observed relation between the  $\eta$  value and an expansion parameter  $m$ , which is an alternative parameter indicating the evolutionary phase of SNRs. Note that  $m$  refers to the evolutionary stage at which the SNR currently resides, and it depends not only on the SNR age, but also on other physical parameters (e.g., ambient density, progenitor mass, and total energy of ). The radius of the SNR,  $R$ , and  $m$  are described respectively with

$$R \propto t^m, \quad (8)$$

and

$$m \equiv \frac{v_{\text{obs}}}{R/t_{\text{age}}}, \quad (9)$$

where  $v_{\text{obs}}$  is the observed expansion velocity.  $m = 1$  indicates the earliest evolutionary stage (also known as the free expansion phase or the ejecta dominated (ED) phase).  $m = 0.4$  corresponds to the Sedov stage at which the SNR continues to expand self-similarly. As the SNRs evolve from  $m = 1$  to 0.4,  $\eta$  decreases to reach  $\sim 1$  in Figure 5 (right). We also fit the observed  $m$ - $\eta$  diagram using an experimental model given by

$$\eta = C_m m^{\delta_m}. \quad (10)$$

The best-fit values were  $C_m = 5.2 \pm 1.0$  and  $\delta_m = 4.0 \pm 0.8$ . The correlation coefficient of the logarithm plots in Figure 5 (right) was approximately 0.60 with a significance of  $1.9\sigma$ . Using the average value of the  $\eta$  parameter, we obtained  $C_m = 3.3 \pm 0.4$  and  $\delta_m = 0.67 \pm 0.34$  and a correlation coefficient of 0.52 with a significance of  $1.6\sigma$ .

Here we summarize the results of 6 SNRs (G1.9+0.3, Cassiopeia A (the SE and NE regions), SN 1006 (the NE and SW regions), RX J1713.7-3946, Vela Jr., and SN 1987A) which were analyzed with the available *NuSTAR* data. Although the analysis using only the *Chandra* is reliable to some extent, the *NuSTAR* observation in the higher X-ray domain enables us to derive the more robust result. When we reduce to those 6 SNRs, the best-fit parameters are  $(C_{\text{age}}, \delta_{\text{age}}) = (1.5 \pm 0.3, 0.41 \pm 0.09)$  with  $\chi^2$  of 16 ( of 3) and  $(C_m, \delta_m) = (5.3 \pm 0.7, 7.7 \pm 1.2)$  with  $\chi^2$  of 6.1, which are roughly consistent with those derived by using all SNRs.

#### 4.2.2. Supernova explosion type

In this subsection, we present the  $\eta$  values from two types of SNe: Type Ia SN which is driven by a thermonuclear explosion of a white dwarf star and Type II which is a core-collapse explosion. In general, the ambient interstellar medium of a Type Ia SNR is rarefied, whereas the circumstellar medium surrounding a core-collapse SNR is clumpy and complex due to stellar wind from the massive progenitor star.

In this paper, G1.9+0.3, Kepler, Tycho, SN 1006, and RCW 86 are classified as Type Ia, and Cassiopeia A, G330.2+1.0, RX J1713.7-3946, Vela Jr., HESS J1731-347, and SN 1987A are classified as core-collapse SNRs. We group SNRs with as Type II. It should be noted that this might not be a precise classification. Figure 6 shows age- $\eta$  and  $m$ - $\eta$  diagrams of Type Ia (top) and Type II (bottom). The best-fit parameters are  $(C_{\text{age}}, \delta_{\text{age}}) = (0.85 \pm 0.55, 1.5 \pm 0.5)$  for Type Ia and  $(C_{\text{age}}, \delta_{\text{age}}) = (1.4 \pm 0.3, 0.41 \pm 0.09)$  for Type II. If we took the averaged  $\eta$ ,  $(C_{\text{age}}, \delta_{\text{age}}) = (4.4 \pm 0.6, -0.29 \pm 0.17)$  for Type Ia and  $(C_{\text{age}}, \delta_{\text{age}}) = (1.8 \pm 0.2, 0.40 \pm 0.07)$  for Type II. As seen in Figure 6 and Table 3, the observed  $\eta$  value of Type Ia SNRs does not have a significant correlation with the age nor the expansion parameter, while Type II SNRs show the relatively strong correlation. Overall,  $\eta$  of core-collapse SNRs appears smaller than that of Type Ia SNRs at  $t_{\text{age}} \lesssim 10000$  years. We should be careful regarding the small number of data samples and the fact that Type II SNRs presented here consist of relatively older SNRs.

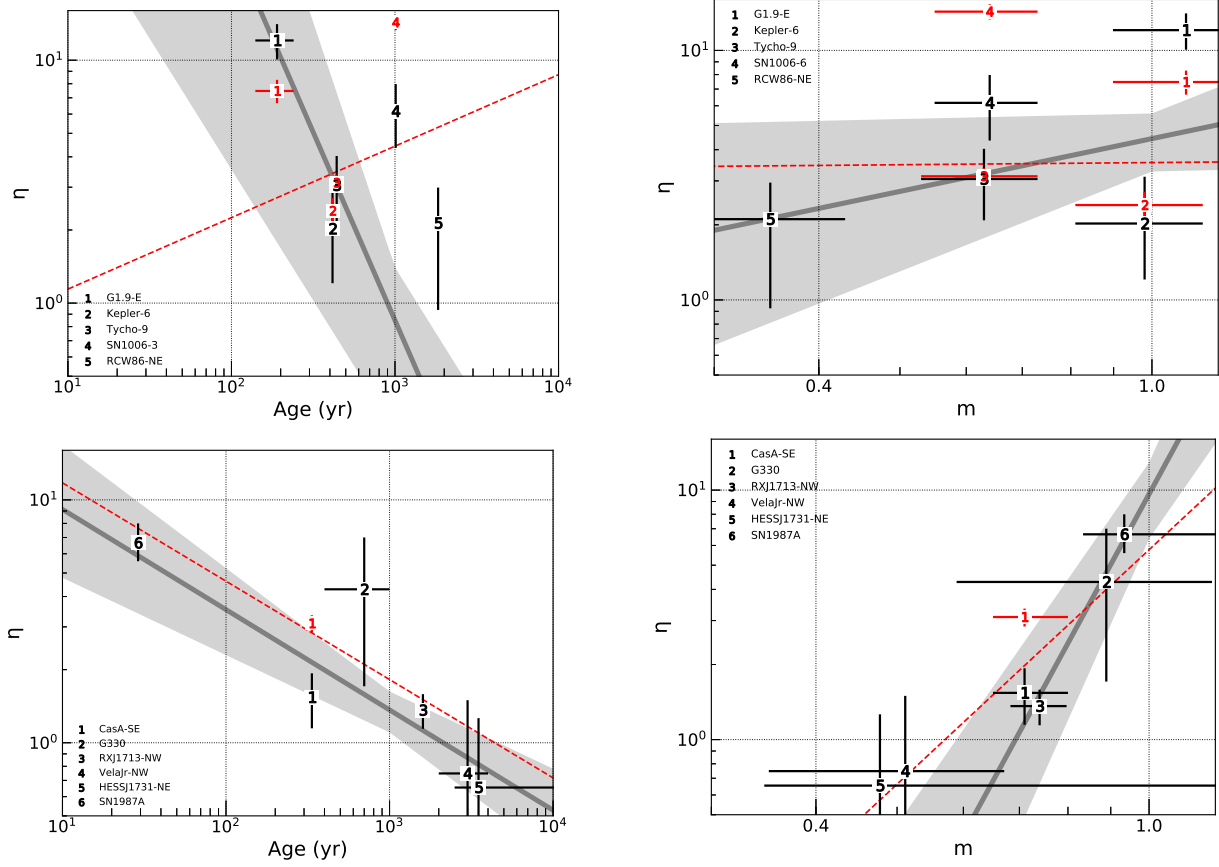


**Figure 6.** Same as Figure 5 for Type I (top) and Type II (bottom).

**Table 3.** Parameters of evolution of  $\eta$  (Equation 7 and Equation 10)

	$C_{\text{age}}$	$\delta_{\text{age}}$	$\chi^2$ (dof)	$\rho^{(a)}$	$C_m$	$\delta_m$	$\chi^2$ (dof)	$\rho^{(a)}$
All SNRs	$1.5 \pm 0.2$	$0.41 \pm 0.08$	17 (8)	$-0.70$ ( $2.4\sigma$ )	$5.2 \pm 1.0$	$4.0 \pm 0.8$	19 (8)	$0.60$ ( $1.9\sigma$ )
All SNRs with averaged $\eta$	$2.2 \pm 0.2$	$0.37 \pm 0.06$	89 (8)	$-0.65$ ( $2.2\sigma$ )	$3.3 \pm 0.4$	$0.67 \pm 0.34$	118 (8)	$0.52$ ( $1.6\sigma$ )
Type Ia	$0.85 \pm 0.55$	$1.5 \pm 0.5$	6.8 (2)	$-0.53$ ( $0.9\sigma$ )	$4.4 \pm 1.2$	$0.69 \pm 0.63$	11 (2)	$0.50$ ( $0.86\sigma$ )
Type Ia with averaged $\eta$	$4.4 \pm 0.6$	$-0.29 \pm 0.17$	75 (2)	$-0.17$ ( $0.27\sigma$ )	$3.5 \pm 0.4$	$0.023 \pm 0.30$	77 (2)	$0.32$ ( $0.5\sigma$ )
Type II	$1.4 \pm 0.3$	$0.41 \pm 0.09$	2.5 (3)	$-0.86$ ( $2.2\sigma$ )	$9.6 \pm 3.2$	$6.2 \pm 1.3$	1.6 (3)	$0.95$ ( $2.9\sigma$ )
Type II with averaged $\eta$	$1.8 \pm 0.2$	$0.40 \pm 0.07$	1.9 (3)	$-0.90$ ( $2.4\sigma$ )	$5.8 \pm 2.2$	$3.1 \pm 1.2$	19 (3)	$0.94$ ( $2.8\sigma$ )

NOTE—<sup>(a)</sup> Pearson's correlation coefficient.

## 5. DISCUSSION

### 5.1. Variety in $v_{\text{sh}} - \varepsilon_0$

First, we summarize the properties of particle acceleration in the individual sources. Significant variations across the remnants were confirmed in G1.9+0.3, Cassiopeia A, Kepler, Tycho, and SN 1006 (see also Tsuji et al. 2019, for the NW of RX J1713.7–3946). Spatially resolved studies could not be conducted in the other SNRs due to lacking the observational data. Figure 7 shows the  $v_{\text{sh}} - \varepsilon_0$  scatter plots of the former five SNRs, which showed significant varieties, indicating four types of  $v_{\text{sh}} - \varepsilon_0$  dependencies. In G1.9+0.3, the cutoff energy parameters showed small variations, but

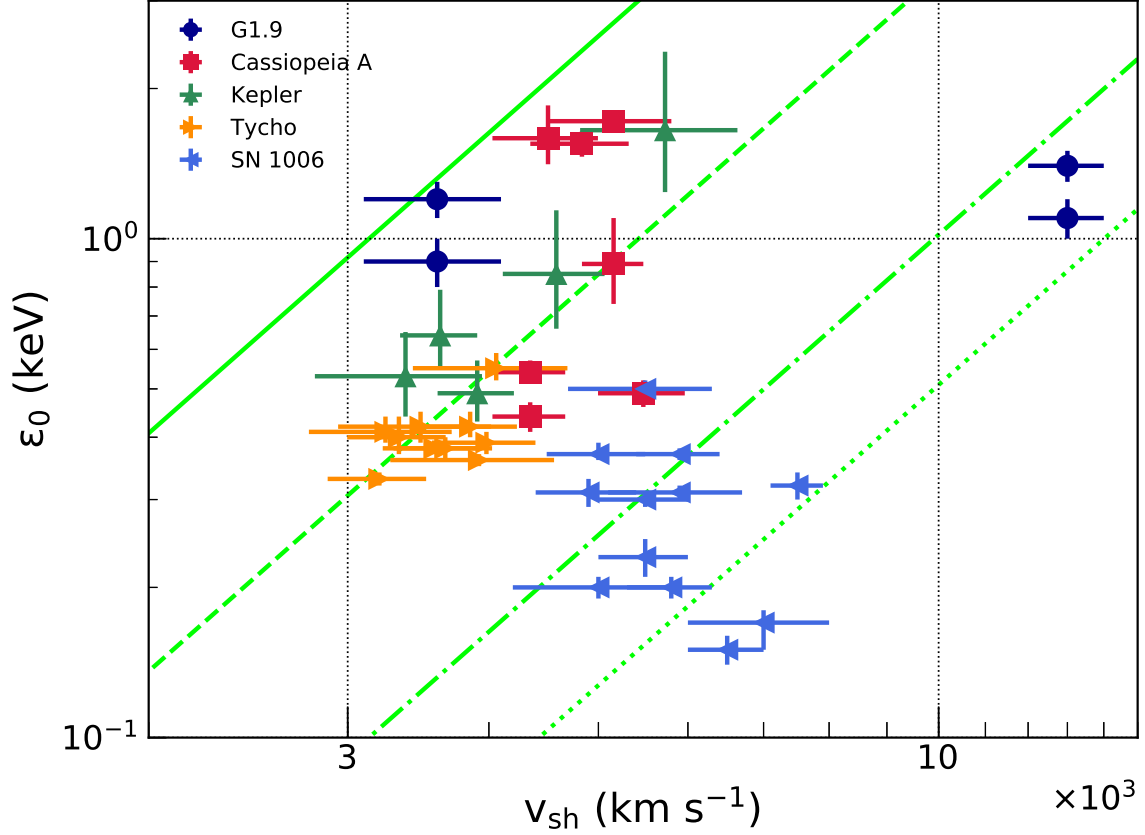


**Figure 7.**  $v_{\text{sh}}-\varepsilon_0$  scatter plots of the synchrotron-dominated regions in G1.9+0.3, Cassiopeia A, Kepler, Tycho (except for *knot g*), and SN 1006. Green solid, dashed, dash-dotted, and dotted lines indicate  $\eta$  of 1, 3, 10, and 20, respectively.

the shock speeds were different from region to region. This was opposite to the case of Cassiopeia A, which the cutoff energy parameters were variable, whereas the shock speeds were nearly constant. Only Kepler and Tycho (except for *knot g*) presented the  $v_{\text{sh}}-\varepsilon_0$  scatter plots nicely described with the theoretical prediction of  $\varepsilon_0 \propto v_{\text{sh}}^2$ . Finally, SN 1006 showed a slightly inverse trend, in which the cutoff energy parameters tended to be smaller in the higher shock-speed regions.

These features were interpreted as follows. Particle acceleration in Kepler and Tycho exhibited the theoretically predicted  $v_{\text{sh}}-\varepsilon_0$  relation. Therefore, the standard framework was applicable in these two SNRs. However, in the other SNRs in which the observed  $v_{\text{sh}}-\varepsilon_0$  plots were not described by the theoretical curve, particle acceleration may have been strongly affected by the surrounding environment. In the case of SN 1006, particle acceleration was probably determined by the ambient magnetic field, because the resulting Bohm factors were correlated with the shock obliquities (see Figure 4 and also Miceli et al. 2009). For G1.9+0.3, the different shock speeds may have been caused by differences in the ambient density, resulting in variable Bohm factors across the remnant. It is more likely that G1.9+0.3, at the age of  $\sim 190$  years, is too young to accelerate sufficiently energetic particles, and our framework of the cooling-limited electron is not appropriate. Instead, the particle acceleration in G1.9+0.3 might be limited by the age. Finally, in the case of Cassiopeia A, the acceleration efficiency might be related to thermal emission (Tsuji 2020). The investigation of the nonthermal and thermal components will be discussed in the separated paper.

## 5.2. Evolution of $\eta$

The evolution of acceleration efficiency, as previously mentioned and shown in Figure 5, was observationally revealed for the first time in this study. The Bohm factor  $\eta$  characterizes the diffusion coefficient and is explicitly related to

the magnetic turbulence.  $\eta$  can also be described as:

$$\eta \equiv \left( \frac{B_0}{\delta B} \right)^2, \quad (11)$$

where  $B_0$  and  $\delta B$  are the initial background magnetic field and the turbulent magnetic field, respectively. A higher value of  $\eta$  (i.e., a larger diffusion coefficient) implies that insufficient turbulent magnetic field to scatter the particles exists. A lower value of  $\eta$  (i.e., a smaller diffusion coefficient) implies that the magnetic field is sufficiently turbulent. The observed age- $\eta$  plots may suggest generation of the turbulent magnetic field is related to the evolution of SNRs: Figure 5 implies the turbulence of magnetic field growing with time. Here we address some open issues, such as a quantitative explanation and a physical meaning of the growth index of  $-\delta$ .

The acceleration efficiency depends on a Mach number of the shock wave, as studied in Caprioli & Spitkovsky (2014a,b,c) using numerical simulations. Caprioli & Spitkovsky (2014c) derived the relation (Eq. (16) therein),

$$\eta \propto \mathcal{M}^{-1/2}, \quad (12)$$

where  $\mathcal{M}$  is the Mach number of the SNR shock. However, the Mach number decreases with the evolution of SNRs because the shock is decelerated, and  $\eta$  increases following Equation 12. Thus, the theoretical  $\mathcal{M}$ - $\eta$  relation predicts the opposite tendency of the observation.

The shock obliquity ( $\theta_{\text{Bn}}$ ) also plays a critical role in particle acceleration in SNRs (Petruk et al. 2011; Caprioli & Spitkovsky 2014a). Whether the acceleration occurs at parallel ( $\theta_{\text{Bn}} \sim 0^\circ$ ) or perpendicular ( $\theta_{\text{Bn}} \sim 90^\circ$ ) shocks remains controversial. Some numerical calculations have suggested a quasi-parallel shock produces particle injection more efficiently and generates a more amplified magnetic field (e.g., Caprioli & Spitkovsky 2014a). They found that acceleration efficiency ( $\varepsilon_{\text{cr}}$ )<sup>3</sup> drastically drops off for  $\theta_{\text{Bn}} \geq 45^\circ$ . SN 1006 is the only target to investigate the dependence on shock obliquity, as we have known the direction of the field. Although one should be cautious about the different definitions of acceleration efficiency, our result also indicates inefficiency (larger  $\eta$ ) above  $\sim 50^\circ$  for shock obliquity in SN 1006, as shown in Figure 4. The observed gradual decrease of acceleration efficiency for increasing  $\theta_{\text{Bn}}$  might be consistent with the simulation result with a higher Mach number, for example  $\mathcal{M} = 50$ . From a morphological point of view, G1.9+0.3 and Vela Jr. resemble bilateral structures similar to SN 1006, but shock obliquities are unknown. If the initial ambient field is aligned, the acceleration efficiency could depend on the shock obliquity in the earlier phase, as confirmed in SN 1006. In the later evolution stage or in the preexisting randomly turbulent field, the shock obliquity is averaged over the outer rim, resulting in efficient acceleration.

Another possible explanation for the mismatch between the measured and theory predicted values of  $\eta$  is a nonlinear modification of the shock profile. In the test-particle limit, the shock front is presumed to be a sharp jump. Considering the backreaction of accelerated particles, the jump profile is modified, and this may have a considerable impact on the acceleration regime (see, for example, Reynolds 2008, for a review of SNRs and references therein). For fast shock waves in young SNRs, this nonlinear effect is not important. However, for slow shocks in older SNRs, the nonlinear effect becomes non-negligible, which might change the acceleration efficiency.

It should be noted that the observed age- $\eta$  plot is somewhat biased because of a selection problem in systematical analyses. There might exist SNRs with larger Bohm factors at the older ages (a few 1,000 years), but their synchrotron emission cannot be detected due to the inefficient acceleration. At that point, the age- $\eta$  plot here is considered as the lower limit of  $\eta$  as a function of age. Our analysis disfavors efficient acceleration with  $\eta \sim 1$  in young SNRs (of a few 100 years).

### 5.2.1. Maximum attainable energy

Evolving acceleration efficiency, as confirmed in Figure 5, would modify a picture of the maximum attainable energy of accelerated particles in SNRs. Because the energy loss timescale for protons is significantly longer than the age of SNR at the earlier evolutionary phase, the maximum energy of the proton is expected to be limited by its age. With the governing equation of  $\tau_{\text{acc}} = \tau_{\text{age}}$ , the maximum energy of the accelerated proton is derived as

$$E_{\text{max,age}} = \frac{3}{20} \frac{q}{c} t v_{\text{sh}}^2 B \eta^{-1}. \quad (13)$$

<sup>3</sup>  $\varepsilon_{\text{cr}}$  is defined as the fraction of the postshock energy density of particles with energies greater than a certain threshold energy. This is different from our definition of acceleration efficiency with the Bohm factor,  $\eta$ .



We simply assume that the shock velocity is constant in the ED phase and is given by a self-similar solution in the Sedov-Taylor (ST) phase:

$$v_{\text{sh}}(t) \propto \begin{cases} t^0 & (\text{ED}) \\ t^{-3/5} & (\text{ST}). \end{cases} \quad (14)$$

Note that sophisticated analytical solutions to express a smooth connection between the ED and ST phases have been well studied (e.g., Truelove & McKee 1999; Tang & Chevalier 2017). Since the evolution of the magnetic field is not well understood, we presume that  $B$  is dependent on the evolutionary age as

$$B(t) \propto t^{-\mu}. \quad (15)$$

Our analysis (see in Figure 5) suggests that the  $\eta$  value also depends on the time evolution of the SNR. Thus, we apply

$$\eta(t) \propto t^{-\delta}. \quad (16)$$

We assume that this empirical relation holds until  $\eta$  becomes unity with  $\delta$  being  $\sim 0.4$  (Equation 7). Substituting into Equation 13, we obtain time dependence on the maximum energy of the proton:

$$E_{\text{max,age}} \propto \begin{cases} t^{1-\mu+\delta} & (\text{ED}) \\ t^{-1/5-\mu+\delta} & (\text{ST}) \end{cases}. \quad (17)$$

Equation 17 insists that  $E_{\text{max,age}}$  can be greater than expected before because of the newly added term of  $\delta$ . Our result,  $\delta \sim 0.4$ , suggests that  $E_{\text{max,age}}$  increases as  $t^{0.2}$  even in the ST stage on the assumption of  $\mu = 0$ .

Let us demonstrate the prediction of Equation 17 for the case of Cassiopeia A. The GeV gamma-ray spectrum from this SNR seems to show a  $\pi^0$  bump that is a characteristic feature of the hadronic scenario. The gamma-ray spectrum shows exponential cutoff at  $\sim 2$  TeV, which roughly translates into the proton spectrum cutoff energy of 20 TeV (Abeysekara et al. 2020). Cassiopeia A is obviously not a PeVatron in the current stage with its age of  $\sim 300$  years. Our measurements showed that in Cassiopeia A  $\eta$  varies from 1 to 6 depending on the site, and the averaged  $\eta$  is about 3. We adopt the averaged value here since the gamma-ray observation could not spatially resolve the exact location of the gamma-ray emission. If we apply  $\delta = 0.4$  and  $\mu = 0$  for the ED (ST) phase of Equation 17, the maximum energy of the proton becomes  $\sim 400$  TeV ( $\sim 30$  TeV) at  $\sim 3000$  years when the  $\eta$  value reaches 1 according to Figure 5 and Equation 7. This maximum energy is approximately twice as large as that in the same later stage with  $\delta = 0$ , which has been sometimes assumed. The time evolution of  $\eta$  may suggest that there would be a possibility for SNRs to become more efficient accelerators of multi-TeV particles at the late stage of  $\gtrsim 1$  kyr. This can be consistent with the evolution of the gamma-ray radiation, which the  $\sim$ kyr SNRs appeared to be strong TeV gamma-ray emitters (Funk 2015). However, it should be emphasised that the assumption above is the most optimistic, and that the maximum energy would be predominantly dependent on other parameters, such as the shock velocity, the magnetic field, and the condition of escape.

Observational studies of  $\eta$  in the later stage of SNRs remain as a future work. The SNRs we analyzed in this study included those in both ED and ST phases, but most of them were relatively young and might be in the very transition stage from ED to ST. Altogether, they indicate the Bohm factor decreases until it becomes close to unity. Our work could not fully determine the behavior of  $\eta$  in the later phase, particularly the phase that has significantly entered into the ST stage. It is also interesting but challenging to measure the  $\eta$  value of escaping particles from the SNRs.

### 5.2.2. Supernova explosion type

Figure 6 showed that Type II SNRs tend to have the lower value of  $\eta$ . Since a core-collapse (Type II) SNR has exploded in the surroundings produced by stellar wind of the massive progenitor, the ambient medium is more irregular and complex than that of Type I. If the obtained evolution of  $\eta$  represents the growth of turbulence, the complexity of the circumstellar medium of a Type II SNR is expected to make the turbulent production faster, which might be observed as smaller  $\eta$  value of Type II. This would be investigated in the future by measurements of the cutoff energy and shock speed with higher accuracy, which can help us reduce the uncertainty of  $\eta$  and distinguish the difference between Type I and II SNRs.

## 6. CONCLUSIONS

We analyzed X-ray observations of 11 young SNRs to determine the cutoff energy parameter in the synchrotron spectrum and constrain the corresponding Bohm factor of each SNR. Our model of synchrotron radiation is based on the framework that the accelerated electron is limited by synchrotron cooling and Bohm diffusion. This assumption is reasonable for SNRs older than 1,000 years if  $B \geq 10\text{--}20\ \mu\text{G}$  and for SNRs as young as a few 100 years if  $B \geq 30\text{--}40\ \mu\text{G}$ . We should be cautious about G1.9+0.3 (150–190 years) and SN 1987A (30 years) because  $B$  should be much larger for the assumption to be valid in these sources, and it is questionable for such young SNRs to be capable of amplifying magnetic fields in their short lifetimes.

The  $v_{\text{sh}}\text{--}\varepsilon_0$  relations obtained for the five individual SNRs are interpreted as the following cases:

1. The  $v_{\text{sh}}\text{--}\varepsilon_0$  scatter plot is nicely represented by the theoretical curve,  $\varepsilon_0 \propto v_{\text{sh}}^2 \eta^{-1}$ , with constant  $\eta$  throughout the remnant in the cases of Kepler and Tycho.
2. Cassiopeia A showed variable cutoff energy parameters but nearly constant shock velocities, resulting in different acceleration efficiency depending on the sites.
3. The acceleration is affected by a surrounding magnetic-field configuration in the case of SN 1006: the  $\eta$  parameters is small near the polar limbs where quasi-parallel shocks are expected to form.
4. The different  $\eta$  values are attributed to the different shock speeds in the case of the youngest SNR in our Galaxy, G1.9+0.3.

With all 11 SNRs together, including G330.2+1.0, RX J1713.7–3946, RCW 86, Vela Jr., HESS J1731–347, and SN 1987A, the systematic tendency of the Bohm factor has been unveiled for the first time. The  $\eta$  in the maximum- $\varepsilon_0$  (or maximum- $v_{\text{sh}}$ ) region of each SNR depends on the evolutionary age as  $\eta = 1.5(t_{\text{age}}/1\ \text{kyr})^{-0.41}$  or on the expansion parameter as  $\eta = 5.2m^{4.0}$ . This can be related to the turbulent generation: the turbulence becomes more self-generated as particles become more accelerated with time. Comparing the time dependence on  $\eta$  between Types I and II supernova explosions, Type II shows a relatively lower  $\eta$  value and a flatter rate of the growth, which might suggest that Type II SNRs exploded in the more complex surroundings of the and could facilitate the turbulence to grow faster. Finally, if we consider the time dependence on  $\eta$  as  $\eta \propto t^{-\delta}$  with  $\delta \approx 0.4$ , which has not been expected before, and assume this condition holds until  $\eta$  reaches unity even in the Sedov-Taylor phase, the attainable maximum energy appears greater by the term of  $\delta$ , possibly in the multi-TeV range.

## ACKNOWLEDGMENTS

The scientific results reported in this paper are based on observations made by the *Chandra* X-ray Observatory. This work was also made use of data from the *NuSTAR* mission, a project led by the California Institute of Technology, managed by the Jet Propulsion Laboratory, and funded by the National Aeronautics and Space Administration. We appreciate the *NuSTAR* Operations, Software, and Calibration teams for support with the execution and analysis of these observations. N.T. is supported by the Japan Society for the Promotion of Science (JSPS) KAKENHI grant No. JP17J06025. This work was partially supported by JSPS KAKENHI grant Nos. JP18H03722 and JP18H05463.

*Software:* NuSTARDAS (v1.4.1), HEASoft (v6.19), nuskybgd (<https://github.com/NuSTAR/nuskybgd>; Wik et al. (2014)), XSPEC (v12.9.0, Arnaud (1996)), CIAO (v4.9, Fruscione et al. (2006))

## APPENDIX

### A. DATASET

The dataset of archival observations of *Chandra* and *NuSTAR* are listed in Table 4 and Table 5, respectively.

**Table 4.** Log of *Chandra* observations

Name	Obs ID	Effective time	Date	RA	Dec	Roll
		(ks)	(yyyy-mm-dd)	(deg)	(deg)	(deg)
G1.9+0.3	6708	23.9	2007-02-10	267.2	-27.2	91.8
G1.9+0.3	8521	25.7	2007-03-03	267.2	-27.2	91.8
G1.9+0.3	10111	68.3	2009-07-23	267.2	-27.2	270.0
G1.9+0.3	10112	50.8	2009-07-18	267.2	-27.2	283.2
G1.9+0.3	10928	35.4	2009-07-13	267.2	-27.2	270.2
G1.9+0.3	10930	82.1	2009-07-26	267.2	-27.2	270.0
G1.9+0.3	12689	155.6	2011-07-14	267.2	-27.2	277.3
G1.9+0.3	12690	48.2	2011-05-16	267.2	-27.2	79.2
G1.9+0.3	12691	184.0	2011-05-09	267.2	-27.2	79.2
G1.9+0.3	12692	162.6	2011-05-12	267.2	-27.2	79.2
G1.9+0.3	12693	127.5	2011-05-18	267.2	-27.2	79.2
G1.9+0.3	12694	159.3	2011-05-20	267.2	-27.2	79.2
G1.9+0.3	12695	39.5	2011-05-23	267.2	-27.2	79.2
G1.9+0.3	13407	48.4	2011-07-18	267.2	-27.2	277.3
G1.9+0.3	13509	55.3	2011-07-22	267.2	-27.2	277.3
G1.9+0.3	16947	38.8	2015-05-04	267.2	-27.2	86.7
G1.9+0.3	16948	39.6	2015-07-14	267.2	-27.2	271.6
G1.9+0.3	16949	9.1	2015-05-20	267.2	-27.2	75.2
G1.9+0.3	17651	111.6	2015-05-05	267.2	-27.2	86.7
G1.9+0.3	17652	26.2	2015-05-09	267.2	-27.2	86.7
G1.9+0.3	17663	56.5	2015-07-24	267.2	-27.2	271.6
G1.9+0.3	17699	19.8	2015-07-17	267.2	-27.2	271.6
G1.9+0.3	17700	14.9	2015-08-31	267.2	-27.2	260.2
G1.9+0.3	17702	36.9	2015-07-15	267.2	-27.2	271.6
G1.9+0.3	17705	9.9	2015-07-25	267.2	-27.2	271.6
G1.9+0.3	18354	29.7	2015-09-01	267.2	-27.2	260.2
(total)		1659.6				
Cassiopeia A	4634	148.6	2004-04-28	350.9	58.8	59.2
Cassiopeia A	4635	135.0	2004-05-01	350.9	58.8	59.2
Cassiopeia A	4636	143.5	2004-04-20	350.9	58.8	49.8
Cassiopeia A	4637	163.5	2004-04-22	350.9	58.8	49.8
Cassiopeia A	4638	164.5	2004-04-14	350.9	58.8	40.3
Cassiopeia A	4639	79.0	2004-04-25	350.9	58.8	49.8
Cassiopeia A	5196	49.5	2004-02-08	350.9	58.8	325.5
Cassiopeia A	5319	42.3	2004-04-18	350.9	58.8	49.8
Cassiopeia A	5320	54.4	2004-05-05	350.9	58.9	65.1
(total)		980.3				
Kepler	116	48.8	2000-06-30	262.7	-21.5	261.1
Kepler	4650	46.2	2004-10-26	262.7	-21.5	268.8
Kepler	6714	157.8	2006-04-27	262.7	-21.4	89.0
Kepler	6715	159.1	2006-08-03	262.7	-21.5	265.7
Kepler	6716	158.0	2006-05-05	262.7	-21.4	89.5
Kepler	6717	106.8	2006-07-13	262.7	-21.5	264.2
Kepler	6718	107.8	2006-07-21	262.7	-21.5	264.8
Kepler	7366	51.5	2006-07-16	262.7	-21.5	264.2
Kepler	16004	102.7	2014-05-13	262.7	-21.5	92.7
Kepler	16614	36.4	2014-05-16	262.7	-21.5	92.7
(total)		975.1				
Tycho	7639	108.9	2007-04-23	6.3	64.1	29.2
Tycho	8551	33.3	2007-04-26	6.3	64.1	29.2
Tycho	10093	118.4	2009-04-13	6.3	64.1	29.2
Tycho	10094	90.0	2009-04-18	6.3	64.1	29.2

Table 4 continued on next page

**Table 4** (*continued*)

Name	Obs ID	Effective time	Date	RA	Dec	Roll
		(ks)	(yyyy-mm-dd)	(deg)	(deg)	(deg)
Tycho	10095	173.4	2009-04-23	6.3	64.1	29.2
Tycho	10096	105.7	2009-04-27	6.3	64.1	29.2
Tycho	10097	107.4	2009-04-11	6.3	64.1	26.3
(total)		737.1				
G330.2+1.0	6687	50.0	2006-05-21	240.2	-51.6	3.3
G330.2+1.0	19163	74.1	2017-05-02	240.2	-51.6	30.2
G330.2+1.0	20068	74.1	2017-05-05	240.2	-51.5	30.2
(total)		198.2				
SN 1006 N	13743	92.6	2012-04-28	225.8	-41.7	19.9
SN 1006 NE	9107	68.9	2008-06-24	226.0	-41.9	280.4
SN 1006 NE	732	68.1	2000-07-10	226.0	-41.9	280.2
SN 1006 SW	13739	100.1	2012-05-04	225.6	-42.1	9.1
SN 1006 NW	1959	89.0	2001-04-26	225.6	-41.8	30.2
SN 1006 NW	13737	87.1	2012-04-20	225.6	-41.8	31.7
SN 1006 W	13738	73.5	2012-04-23	225.4	-42.0	25.3
SN 1006 W	14424	25.4	2012-04-27	225.4	-42.0	25.3
SN 1006 SE	13741	98.5	2012-04-25	226.0	-42.0	24.6
SN 1006 S	13742	79.0	2012-06-15	225.8	-42.1	289.1
(total)		782.2				
RX J1713.7–3946 NW	736	29.6	2000-07-25	258.0	-39.6	282.5
RX J1713.7–3946 NW	6370	29.8	2006-05-03	257.9	-39.6	64.8
RX J1713.7–3946 NW	10090	28.4	2009-01-30	257.9	-39.5	98.6
RX J1713.7–3946 NW	10091	29.6	2009-05-16	257.9	-39.5	53.8
RX J1713.7–3946 NW	10092	29.2	2009-09-10	257.9	-39.6	266.1
RX J1713.7–3946 NW	12671	89.9	2011-07-01	257.9	-39.6	304.5
(total)		236.5				
RCW 86	1993	92.0	2001-02-01	220.2	-62.7	80.2
RCW 86 NE	4611	71.7	2004-06-15	221.3	-62.4	295.2
RCW 86 NE	7642	69.2	2007-06-20	221.3	-62.3	299.0
RCW 86	10699	2.0	2009-06-14	220.5	-62.6	304.4
RCW86	13748	36.1	2013-02-14	220.1	-62.7	70.7
RCW 86	14890	26.7	2013-02-03	220.4	-62.2	75.2
RCW 86	15608	29.2	2013-02-05	220.4	-62.2	75.2
RCW 86	15609	37.6	2013-02-10	220.4	-62.2	75.2
RCW86	15610	23.1	2013-02-17	220.1	-62.7	70.7
RCW86	15611	25.9	2013-02-12	220.1	-62.7	70.7
RCW 86 NE	16952	67.2	2015-06-25	221.3	-62.4	293.6
(total)		480.7				
Vela Jr. NW	3846	39.5	2003-01-05	132.3	-45.6	30.2
Vela Jr. NW	4414	34.5	2003-01-06	132.3	-45.6	30.2
Vela Jr. NORTH	9123	39.7	2008-08-31	132.3	-45.7	146.2
(total)		113.7				
HESS J1731–347	9139	29.2	2008-04-28	263.0	-34.7	81.2
SN 1987A	14697	67.6	2013-03-21	83.9	-69.3	264.2
SN 1987A	14698	68.5	2013-09-28	83.9	-69.3	79.4
SN 1987A	15809	70.5	2014-03-19	83.9	-69.3	266.1
SN 1987A	15810	48.3	2014-09-20	83.9	-69.3	84.2
SN 1987A	17415	19.4	2014-09-17	83.9	-69.3	84.2
(total)		274.2				

**Table 5.** Log of *NuSTAR* observations

Name	Obs ID	Effective time	Date	RA	Dec	Roll
		(ks)	(yyyy-mm-dd)	(deg)	(deg)	(deg)
G1.9+0.3	40001015003	85.4	2013-07-08	267.2	−27.2	327.3
G1.9+0.3	40001015005	121.6	2013-07-14	267.2	−27.2	327.3
G1.9+0.3	40001015007	144.7	2013-07-27	267.2	−27.2	327.3
(total)		351.7				
Cassiopeia A	40021002002	270.9	2012-11-23	350.8	58.8	338.3
Cassiopeia A	40021002006	135.6	2013-03-02	350.9	58.8	248.7
Cassiopeia A	40021002008	189.3	2013-03-05	350.9	58.8	248.7
Cassiopeia A	40021003003	197.8	2013-05-28	350.9	58.8	151.2
Cassiopeia A	40021001002	170.1	2012-08-27	350.8	58.8	75.7
Cassiopeia A	40021001004	25.7	2012-10-07	350.7	58.8	33.0
Cassiopeia A	40021001005	184.5	2012-10-07	350.8	58.8	33.0
Cassiopeia A	40021002010	12.4	2013-03-09	350.9	58.8	248.7
Cassiopeia A	40021003002	12.4	2013-05-28	350.9	58.8	151.2
Cassiopeia A	40021011002	235.1	2013-10-30	350.9	58.8	6.8
Cassiopeia A	40021012002	205.8	2013-11-27	350.8	58.8	335.2
Cassiopeia A	40021015002	74.4	2013-12-21	350.9	58.8	312.3
Cassiopeia A	40021015003	136.9	2013-12-23	350.9	58.8	312.2
(total)		1850.9				
SN1006 NE	40110001002	198.5	2016-03-02	225.9	−41.8	180.0
SN1006 SW	40110002002	204.8	2016-03-08	225.5	−42.0	180.0
RX J1713.7−3946 NW	40111001002	43	2015-09-27	257.86	−39.52	343.3
RX J1713.7−3946 NW	40111002002	49	2016-03-30	257.93	−39.58	165.6
(total)		92.0				
Vela Jr. NW	40101011002	69.0	2015-07-07	132.2	−45.7	40.4
Vela Jr. NW	40101011004	102.1	2015-07-16	132.2	−45.7	44.4
(total)		142.2				
SN1987A	40001014002	57.5	2012-09-07	84.0	−69.2	149.1
SN1987A	40001014003	113.3	2012-09-08	84.0	−69.2	149.1
SN1987A	40001014004	198.2	2012-09-11	83.9	−69.2	149.2
SN1987A	40001014006	45.2	2012-10-20	84.0	−69.3	190.5
SN1987A	40001014007	173.2	2012-10-21	83.9	−69.3	190.5
SN1987A	40001014010	160.0	2012-12-12	83.9	−69.3	242.9
SN1987A	40001014013	403.1	2013-06-29	83.8	−69.2	80.1
SN1987A	40001014015	83.5	2014-04-21	83.8	−69.3	13.1
SN1987A	40001014016	379.4	2014-04-22	83.8	−69.3	13.1
SN1987A	40001014018	170.5	2014-06-15	83.8	−69.2	65.0
SN1987A	40001014020	237.4	2014-06-19	83.8	−69.2	70.2
SN1987A	40001014023	397.7	2014-08-01	83.9	−69.2	111.4
(total)		2419.0				

## B. THERMAL PARAMETERS

Table 6 presents parameters of the thermal model which is used for fitting the spectra of Cassiopeia A, Kepler, Tycho, SN 1006, RCW 86, and SN 1987A in addition to the synchrotron radiation model (see Table 2 for the nonthermal parameters).



Table 6. Thermal parameters.

Region	$kT$	O	Ne	Mg	Si	S	Ar	Ca	Fe	$nt$	Norm
	(keV)	(O <sub>⊙</sub> )	(Ne <sub>⊙</sub> )	(Mg <sub>⊙</sub> )	(Si <sub>⊙</sub> )	(S <sub>⊙</sub> )	(Ar <sub>⊙</sub> )	(Ca <sub>⊙</sub> )	(Fe <sub>⊙</sub> )	(10 <sup>10</sup> s cm <sup>-3</sup> )	(10 <sup>-5</sup> cm <sup>-5</sup> )
<b>Cassiopeia A</b>											
N1	1.70	1.0	1.0	1.0 ± 0.6	11 ± 2	10 ± 2	12 <sup>+7</sup> <sub>-6</sub>	12 <sup>+16</sup> <sub>-12</sub>	1.0	6.9	5.0 ± 0.9
N2	1.70	1.0	1.0	1.8 <sup>+0.5</sup> <sub>-0.4</sub>	7.9 <sup>+1.1</sup> <sub>-0.9</sub>	6.9 <sup>+1.2</sup> <sub>-1.0</sub>	9.5 <sup>+4.2</sup> <sub>-3.9</sub>	8.0 <sup>+10.2</sup> <sub>-8.0</sub>	1.0	6.9	5.0 ± 0.6
S	0.69	1.0	1.0	1.3 ± 0.1	1.1 ± 0.1	1.4 ± 0.2	3.0 <sup>+1.3</sup> <sub>-1.2</sub>	1.0	1.0	22.6	118 <sup>+14</sup> <sub>-13</sub>
NW	1.61	1.0	1.0	0.1 <sup>+2.3</sup> <sub>-0.1</sub>	20 <sup>+36</sup> <sub>-8</sub>	12 <sup>+21</sup> <sub>-5</sub>	42 <sup>+82</sup> <sub>-23</sub>	60 <sup>+129</sup> <sub>-49</sub>	1.0	9.6	1.2 <sup>+0.9</sup> <sub>-0.8</sub>
SE	1.77	1.0	1.0	1.4	6.0	3.3	1.0	1.0	1.0	10.4	1.4 ± 0.4
E	1.84	1.0	1.0	0.5 ± 0.5	4.4 <sup>+1.0</sup> <sub>-0.8</sub>	2.5 <sup>+0.9</sup> <sub>-0.8</sub>	1.0	1.0	1.0	14.3	3.6 <sup>+0.7</sup> <sub>-0.6</sub>
NE	1.76	1.0	1.0	0.8	11.0	8.8	10.2	23.1	1.0	14.0	1.3 ± 0.2
<b>Kepler</b>											
1	0.80	0.42	1.0	1.1	11 ± 1	19 ± 1	1.0	1.0	1.0	5.9	5.8 ± 0.3
2	0.58	0.21	1.0	0.4	15 ± 1	27 ± 3	1.0	1.0	1.0	9.5	12 ± 1
3	0.60	0.98	1.0	0.4	21 ± 2	26 ± 4	1.0	1.0	1.0	82.1	3.9 <sup>+0.4</sup> <sub>-0.3</sub>
4	0.34	1.00	1.0	1.0	1	1.0	1.0	1.0	1.0	100.0	<0.35
5	0.50	1.00	1.0	1.0	1	1.0	1.0	1.0	1.0	60.0	0.28 <sup>+0.43</sup> <sub>-0.28</sub>
6	0.53	1.00	1.0	1.0	44	28	130.8	1.0	1.0	69.8	0.15 ± 0.06
7	0.52	1.00	1.0	1.0	39	29	1.0	1.0	1.0	60.0	0.29 ± 0.07
8	0.45	2.21 <sup>+3.37</sup> <sub>-2.21</sub>	1.0	2.7 <sup>+4.2</sup> <sub>-2.7</sub>	67 <sup>+77</sup> <sub>-29</sub>	105 <sup>+130</sup> <sub>-54</sub>	1.0	1.0	1.0	42.1	0.47 <sup>+0.36</sup> <sub>-0.25</sub>
9	0.57	0.18	1.0	0.4 ± 0.3	18 ± 2	22 ± 4	1.0	1.0	1.0	20.5	3.4 <sup>+0.4</sup> <sub>-0.3</sub>
10	0.57	0.61	1.0	0.4	39 <sup>+6</sup> <sub>-5</sub>	42 <sup>+9</sup> <sub>-7</sub>	15 <sup>+28</sup> <sub>-15</sub>	1.0	1.0	87.1	1.8 ± 0.3
11	0.51	0.18	1.0	0.4	34 <sup>+6</sup> <sub>-5</sub>	43 <sup>+11</sup> <sub>-10</sub>	1.0	1.0	1.0	12.7	1.2 ± 0.2
12	0.50	0.72	1.0	0.7	21 <sup>+7</sup> <sub>-5</sub>	34 <sup>+15</sup> <sub>-10</sub>	62 <sup>+87</sup> <sub>-62</sub>	1.0	1.0	9.7	2.5 <sup>+0.8</sup> <sub>-0.7</sub>
13	0.69	0.59 <sup>+0.08</sup> <sub>-0.07</sub>	1.0	1.0 ± 0.1	7.5 <sup>+0.5</sup> <sub>-0.4</sub>	15 ± 1	34 ± 5	1.0	1.2 ± 0.1	8.2	26 ± 1
14	2.11	0.24 <sup>+0.14</sup> <sub>-0.11</sub>	1.0	2.8 ± 0.3	17 <sup>+2</sup> <sub>-1</sub>	17 ± 2	28 ± 5	1.0	1.0	3.0	2.5 <sup>+0.3</sup> <sub>-0.2</sub>
<b>Tycho</b>											
1	0.78	1.0	1.0	1.0	33 <sup>+4</sup> <sub>-3</sub>	45 <sup>+6</sup> <sub>-5</sub>	129 <sup>+20</sup> <sub>-18</sub>	316 <sup>+67</sup> <sub>-65</sub>	1.0	6.8	20 ± 2
2	2.17	1.9 <sup>+0.3</sup> <sub>-0.2</sub>	1.0	0.8	12 ± 1	11 ± 1	13	18.8	1.0	2.3	30 ± 3
3	3.38	2.3 ± 0.5	1.0	1.0	10 <sup>+3</sup> <sub>-2</sub>	7.2 <sup>+2.3</sup> <sub>-1.7</sub>	1	1.0	1.0	2.3	5.6 <sup>+1.4</sup> <sub>-1.2</sub>
4	5.46	10.9	1.0	1.0	107	68	74	1.0	1.0	2.6	0.94 ± 0.03
5	1.30	2.7 ± 0.4	1.0	1.0	32 ± 4	39 <sup>+6</sup> <sub>-5</sub>	55 <sup>+10</sup> <sub>-9</sub>	129 <sup>+28</sup> <sub>-25</sub>	1.0	3.5	30 <sup>+5</sup> <sub>-4</sub>
6	1.81	6.1 <sup>+2.5</sup> <sub>-1.2</sub>	1.0	1.8 <sup>+1.4</sup> <sub>-0.7</sub>	57 <sup>+50</sup> <sub>-20</sub>	61 <sup>+54</sup> <sub>-22</sub>	1	1.0	1.0	2.9	3.5 <sup>+2.0</sup> <sub>-1.7</sub>
7	2.64	4.0	1.0	3.5	31	23	1	1.0	1.0	3.0	3.6 ± 0.1
8	1.79	1.0	1.0	4.2	107	102	121	276.1	1.0	4.3	0.93 ± 0.03
9	2.52	5.5	1.0	5.1	68 <sup>+21</sup> <sub>-13</sub>	54 <sup>+18</sup> <sub>-11</sub>	65	1.0	1.0	3.2	1.2 ± 0.3
10	1.22	7.1 ± 0.7	1.0	1.2 ± 0.1	20 <sup>+3</sup> <sub>-2</sub>	22 <sup>+4</sup> <sub>-3</sub>	27 <sup>+5</sup> <sub>-4</sub>	60 <sup>+17</sup> <sub>-14</sub>	1.0	3.9	43 <sup>+7</sup> <sub>-6</sub>
11	1.25	5.1 <sup>+1.2</sup> <sub>-1.0</sub>	1.0	1.3 <sup>+0.7</sup> <sub>-0.6</sub>	40 <sup>+12</sup> <sub>-8</sub>	45 <sup>+15</sup> <sub>-10</sub>	87	1.0	1.0	3.6	3.6 ± 0.9
12	1.73	3.2 ± 0.6	1.0	1.4 <sup>+0.6</sup> <sub>-0.5</sub>	32 <sup>+13</sup> <sub>-8</sub>	32 <sup>+14</sup> <sub>-9</sub>	1	1.0	1.0	2.8	3.9 <sup>+1.4</sup> <sub>-1.1</sub>
13	1.64	3.4 <sup>+0.6</sup> <sub>-0.5</sub>	1.0	1.9 ± 0.3	24 ± 2	22	1	1.0	1.0	2.6	5.7 ± 0.4
14	1.95	6.4 ± 0.5	1.0	1.1 ± 0.1	17 <sup>+2</sup> <sub>-1</sub>	13 ± 1	10	13.5	1.0	2.3	32 ± 3
15	0.73 <sup>+0.05</sup> <sub>-0.02</sub>	1.0	1.0	1.0	30 <sup>+6</sup> <sub>-4</sub>	37 <sup>+7</sup> <sub>-6</sub>	36 <sup>+11</sup> <sub>-5</sub>	1.0	1.0	29 <sup>+13</sup> <sub>-12</sub>	22 ± 5
16	0.61	0.8 ± 0.1	1.0	1.9 <sup>+0.2</sup> <sub>-0.1</sub>	18 ± 2	40 ± 4	124 ± 18	1.0	1.0	7.1	37 ± 3
17	1.15 <sup>+0.23</sup> <sub>-0.11</sub>	1.1 <sup>+0.2</sup> <sub>-0.1</sub>	1.0	1.0	23 ± 2	26 <sup>+3</sup> <sub>-4</sub>	46 <sup>+12</sup> <sub>-13</sub>	1.0	1.0	3.0 <sup>+0.5</sup> <sub>-0.6</sub>	32 <sup>+4</sup> <sub>-5</sub>
18	0.77	1.0	1.0	1.3 <sup>+0.4</sup> <sub>-0.3</sub>	46 <sup>+18</sup> <sub>-15</sub>	55 <sup>+22</sup> <sub>-18</sub>	96 <sup>+40</sup> <sub>-34</sub>	329 <sup>+141</sup> <sub>-115</sub>	1.0	5.8	53 <sup>+29</sup> <sub>-15</sub>
19	1.15	1.7	1.0	1.4	38 <sup>+4</sup> <sub>-3</sub>	40 <sup>+4</sup> <sub>-3</sub>	61 ± 9	196 <sup>+30</sup> <sub>-29</sub>	1.0	3.8	18 ± 2
20	1.76	1.6	1.0	2.0	56 <sup>+32</sup> <sub>-15</sub>	49 <sup>+29</sup> <sub>-14</sub>	31	45.6	1.0	3.6	1.9 ± 0.7
<b>SN 1006</b>											
1	0.41	5.0	4.7	12.0	29	1.0	1.0	1.0	1.0	1.6	1.1 <sup>+0.4</sup> <sub>-0.3</sub>
2	0.10 <sup>+0.06</sup> <sub>-0.10</sub>	5.0	4.7	12.0	29	1.0	1.0	1.0	1.0	1.6	63 <sup>+166</sup> <sub>-53</sub>
3	0.38 <sup>+0.08</sup> <sub>-0.09</sub>	4.4	1.5	15.0	50	1.0	1.0	1.0	1.0	1.3	1.5 <sup>+0.5</sup> <sub>-0.4</sub>
4	0.41 <sup>+0.04</sup> <sub>-0.05</sub>	4.4	1.5	15.0	50	1.0	1.0	1.0	1.0	1.3	2.9 <sup>+0.5</sup> <sub>-0.4</sub>
5	0.29 <sup>+0.05</sup> <sub>-0.06</sub>	4.4	1.5	15.0	50	1.0	1.0	1.0	1.0	1.3	2.8 <sup>+1.2</sup> <sub>-0.7</sub>
6	0.37 ± 0.02	4.4	1.5	15.0	50	1.0	1.0	1.0	1.0	1.3	6.1 ± 0.9
7	2.1 <sup>+0.9</sup> <sub>-0.5</sub>	9.0 <sup>+1.4</sup> <sub>-0.9</sub>	1.5	11 <sup>+2</sup> <sub>-1</sub>	44 <sup>+11</sup> <sub>-6</sub>	1.0	1.0	1.0	1.0	0.35 <sup>+0.05</sup> <sub>-0.03</sub>	3.3 <sup>+0.4</sup> <sub>-0.5</sub>
8	1.4 <sup>+0.8</sup> <sub>-0.4</sub>	6.7 <sup>+0.9</sup> <sub>-0.7</sub>	1.5	8.8 <sup>+1.4</sup> <sub>-1.2</sub>	48 <sup>+15</sup> <sub>-12</sub>	1.0	1.0	1.0	1.0	0.47 <sup>+0.11</sup> <sub>-0.07</sub>	10 ± 2
9	0.39 <sup>+0.02</sup> <sub>-0.03</sub>	4.4	1.5	15.0	241 <sup>+63</sup> <sub>-45</sub>	1.0	1.0	1.0	1.0	1.3	13 <sup>+5</sup> <sub>-4</sub>
10	0.40 <sup>+0.04</sup> <sub>-0.03</sub>	4.4	1.5	15.0	50	1.0	1.0	1.0	1.0	1.3	10 <sup>+3</sup> <sub>-2</sub>
11	0.39 ± 0.06	4.4	1.5	15.0	50	1.0	1.0	1.0	1.0	1.3	7.4 <sup>+2.4</sup> <sub>-2.0</sub>
12	0.38 ± 0.06	4.4	1.5	15.0	50	1.0	1.0	1.0	1.0	1.3	4.5 <sup>+1.4</sup> <sub>-1.2</sub>
13	0.12 <sup>+0.16</sup> <sub>-0.12</sub>	5.0	4.7	12.0	29	1.0	1.0	1.0	1.0	1.6	25 <sup>+225</sup> <sub>-22</sub>
14	0.09 <sup>+0.19</sup> <sub>-0.09</sub>	5.0	4.7	12.0	29	1.0	1.0	1.0	1.0	1.6	27 <sup>+62</sup> <sub>-26</sub>

Table 6 continued on next page

Table 6 (continued)

Region	$kT$	O	Ne	Mg	Si	S	Ar	Ca	Fe	$nt$	Norm
	(keV)	( $O_{\odot}$ )	( $Ne_{\odot}$ )	( $Mg_{\odot}$ )	( $Si_{\odot}$ )	( $S_{\odot}$ )	( $Ar_{\odot}$ )	( $Ca_{\odot}$ )	( $Fe_{\odot}$ )	( $10^{10} \text{ s cm}^{-3}$ )	( $10^{-5} \text{ cm}^{-5}$ )
15	$0.14^{+0.15}_{-0.14}$	5.0	4.7	12.0	29	1.0	1.0	1.0	1.0	1.6	$2.6^{+50.4}_{-2.2}$
16	$0.27^{+0.02}_{-0.03}$	$6.3^{+1.3}_{-0.7}$	$4.3^{+0.9}_{-1.0}$	12.0	$342^{+108}_{-88}$	1.0	1.0	1.0	1.0	1.6	$41^{+33}_{-12}$
17	$5.5^{+5.5}_{-3.2}$	$20^{+24}_{-9}$	$13^{+10}_{-4}$	$9.0^{+5.1}_{-3.1}$	29	1.0	1.0	1.0	1.0	$0.12^{+0.24}_{-0.02}$	$1.6^{+1.5}_{-0.7}$
RCW 86											
NE	0.44	1	1.9	1.9	1.9	1	1	1.2	1	2.7	$17 \pm 1$
SN 1987A											
whole	$0.68 \pm 0.03 / 2.5^{+0.3}_{-0.2}$	0.34	3.0	1.0	1.4	2.5	2.7	1	0.61	$8.5^{+2.3}_{-1.7}$	$290 \pm 12 / 50 \pm 4$

NOTE— The parameter values without uncertainties are fixed. For the thermal model, VNEI is used for Cassiopeia A, Kepler, and Tycho, while Vpshock is used for SN 1006 and RCW 86 (see also the text). In SN 1987A, the first and second terms of  $kT$  and Norm indicate the best-fit parameters of the Vequl and Vpshock models, respectively.

## REFERENCES

- Abeyssekara, A. U., Archer, A., Benbow, W., et al. 2020, 894, 51
- Acero, F., Katsuda, S., Ballet, J., & Petre, R. 2017, 597, A106
- Aharonian, F., Sun, X.-n., & Yang, R.-z. 2017, 603, A7
- Allen, G. E., Chow, K., DeLaney, T., et al. 2015, 798, 82
- Arnaud, K. A. 1996, in *Astronomical Society of the Pacific Conference Series*, Vol. 101, *Astronomical Data Analysis Software and Systems v*, ed. G. H. Jacoby & J. Barnes, 17
- Bamba, A., Yamazaki, R., Ueno, M., & Koyama, K. 2003, *The Astrophysical Journal*, 589, 827
- Bamba, A., Yamazaki, R., Yoshida, T., Terasawa, T., & Koyama, K. 2005, 621, 793
- Bell, A. R. 1978, 182, 147
- Berezhko, E. G., & Völk, H. J. 2006, 451, 981
- Boggs, S. E., Harrison, F. A., Miyasaka, H., et al. 2015, *Science*, 348, 670
- Borkowski, K. J., Gwynne, P., Reynolds, S. P., et al. 2017, 837, L7
- Borkowski, K. J., Reynolds, S. P., Green, D. A., et al. 2010, 724, L161
- Borkowski, K. J., Reynolds, S. P., Williams, B. J., & Petre, R. 2018, 868, L21
- Brose, R., Sushch, I., Pohl, M., et al. 2019, arXiv e-prints, arXiv:1906.02725
- Caprioli, D., & Spitkovsky, A. 2014a, 783, 91
- . 2014b, 794, 46
- . 2014c, 794, 47
- Cassam-Chenaï, G., Decourchelle, A., Ballet, J., et al. 2004, 414, 545
- Frank, K. A., Zhekov, S. A., Park, S., et al. 2016, 829, 40
- Fruscione, A., McDowell, J. C., Allen, G. E., et al. 2006, in , 62701V
- Funk, S. 2015, *Annual Review of Nuclear and Particle Science*, 65, 245
- Ghavamian, P., Raymond, J., Hartigan, P., & Blair, W. P. 2000, 535, 266
- Grefenstette, B. W., Harrison, F. A., Boggs, S. E., et al. 2014, 506, 339
- H. E. S. S. Collaboration, Abramowski, A., Acero, F., et al. 2011, 531, A81
- Katsuda, S., Petre, R., Hughes, J. P., et al. 2010a, 709, 1387
- Katsuda, S., Petre, R., Mori, K., et al. 2010b, *The Astrophysical Journal*, 723, 383
- Katsuda, S., Tsunemi, H., & Mori, K. 2008a, 678, L35
- Katsuda, S., Tsunemi, H., Uchida, H., & Kimura, M. 2008b, 689, 225
- Lee, J.-J., Raymond, J. C., Park, S., et al. 2010, 715, L146
- Li, J.-T., Ballet, J., Miceli, M., et al. 2018, 864, 85
- Lopez, L. A., Grefenstette, B. W., Reynolds, S. P., et al. 2015, 814, 132
- Malyshev, D., Pühlhofer, G., Santangelo, A., & Vink, J. 2019, arXiv e-prints, arXiv:1903.03045
- McCray, R., & Fransson, C. 2016, 54, 19
- Miceli, M., Bocchino, F., Decourchelle, A., et al. 2013, *Astronomy & Astrophysics*, 556, A80
- Miceli, M., Bocchino, F., Iakubovskiy, D., et al. 2009, 501, 239
- Park, S., Mori, K., Kargaltsev, O., et al. 2006, 653, L37
- Patnaude, D. J., & Fesen, R. A. 2009, 697, 535
- Petruk, O., Orlando, S., Beshley, V., & Bocchino, F. 2011, 413, 1657
- Reynolds, S. P. 1998, 493, 375
- . 2008, 46, 89
- Reynolds, S. P., Zoglauer, A., Boggs, S. E., Harrison, F., & NuSTAR Team. 2015, in *American Astronomical Society Meeting Abstracts*, Vol. 225, *American Astronomical Society Meeting Abstracts #225*, 140.22
- Reynoso, E. M., Hughes, J. P., & Moffett, D. A. 2013, 145, 104

- Rosado, M., Ambrocio-Cruz, P., Le Coarer, E., & Marcelin, M. 1996, 315, 243
- Rothenflug, R., Ballet, J., Dubner, G., et al. 2004, 425, 121
- Sato, T., Katsuda, S., Morii, M., et al. 2018, 853, 46
- Stage, M. D., Allen, G. E., Houck, J. C., & Davis, J. E. 2006, *Nature Physics*, 2, 614
- Tanaka, T., Uchiyama, Y., Aharonian, F. A., et al. 2008, 685, 988
- Tang, X., & Chevalier, R. A. 2017, 465, 3793
- Truelove, J. K., & McKee, C. F. 1999, 120, 299
- Tsubone, Y., Sawada, M., Bamba, A., Katsuda, S., & Vink, J. 2017, 835, 34
- Tsuji, N. 2020, PhD thesis (Rikkyo University)
- Tsuji, N., & Uchiyama, Y. 2016, 68, 108
- Tsuji, N., Uchiyama, Y., Aharonian, F., et al. 2019, 877, 96
- Vink, J. 2008, 689, 231
- Völk, H. J., Berezhko, E. G., & Ksenofontov, L. T. 2005, *Astronomy & Astrophysics*, 433, 229
- Wik, D. R., Hornstrup, A., Molendi, S., et al. 2014, 792, 48
- Williams, B. J., Borkowski, K. J., Ghavamian, P., et al. 2013, 770, 129
- Williams, B. J., Hewitt, J. W., Petre, R., & Temim, T. 2018, 855, 118
- Winkler, P. F., Williams, B. J., Reynolds, S. P., et al. 2014, 781, 65
- Yamaguchi, H., Katsuda, S., Castro, D., et al. 2016, 820, L3
- Zirakashvili, V. N., & Aharonian, F. 2007, 465, 695